

## TRANSPARENT BOUNDARY CONDITIONS FOR TIME-DEPENDENT PROBLEMS\*

DANIEL RUPRECHT<sup>†</sup>, ACHIM SCHÄDLE<sup>†</sup>, FRANK SCHMIDT<sup>†</sup>, AND  
LIN ZSCHIEDRICH<sup>†</sup>

**Abstract.** A new approach to derive transparent boundary conditions (TBCs) for dispersive wave, Schrödinger, heat, and drift-diffusion equations is presented. It relies on the pole condition and distinguishes between physically reasonable and unreasonable solutions by the location of the singularities of the Laplace transform of the exterior solution. Here the Laplace transform is taken with respect to a generalized radial variable. To obtain a numerical algorithm, a Möbius transform is applied to map the Laplace transform onto the unit disc. In the transformed coordinate the solution is expanded into a power series. Finally, equations for the coefficients of the power series are derived. These are coupled to the equation in the interior and yield transparent boundary conditions. Numerical results are presented in the last section, showing that the error introduced by the new approximate TBCs decays exponentially in the number of coefficients.

**Key words.** transparent boundary condition, nonreflecting boundary condition, pole condition, wave equation, Klein–Gordon equation, Schrödinger equation, drift-diffusion equation

**AMS subject classifications.** 65M60, 65M20, 30E10

**DOI.** 10.1137/070692637

**1. Introduction.** In the simulation of wave propagation phenomena on unbounded domains, transparent boundary conditions are needed in order to make the computational domain finite.

Here we present a new concept based on the pole condition to derive transparent boundary conditions for the dispersive wave equation (Klein–Gordon equation), the Schrödinger equation, and the drift-diffusion equation. The symbol  $p(\partial_t)$  is used to treat all the equations simultaneously:

$$(1.1) \quad p(\partial_t)u(t, x) = \partial_{xx}u(t, x) + 2d\partial_x u(t, x) - k^2(t, x)u(t, x) \text{ for } x \in \mathbb{R}, t \geq 0.$$

The pole condition as presented here is the condition that some function  $U(\tilde{s}, t)$  is analytic on the unit disk. By expanding  $U(\tilde{s}, t)$  into a power series  $\sum_{\ell=0}^{\infty} a_{\ell}(t)\tilde{s}^{\ell}$  and matching moments a system of ordinary differential equations (ODEs) for the coefficients  $a_{\ell}(t)$  is deduced that is coupled to the boundary data of  $u$ . Truncating the power series yields an algorithm to realize transparent boundary conditions. Our approximation of the pole condition is almost equivalent to the approach used by Hohage and Nannen in [18], where it was applied to time-harmonic scattering and eigenvalue problems in one and two space dimensions. In [18] convergence results for the time-harmonic setting are given. The theoretical framework for the transient case is not yet developed.

The pole condition approach shares the variational formulation with transparent boundary conditions based on infinite elements [4] but is nevertheless distinctively different. In the derivation of the pole condition, ansatz and test functions are different, and the ansatz functions do not represent a meaningful solution in the exterior.

---

\*Received by the editors May 22, 2007; accepted for publication (in revised form) March 17, 2008; published electronically July 2, 2008. This work was supported by the DFG Research Center MATHEON “Mathematics for Key Technologies” in Berlin.

<http://www.siam.org/journals/sisc/30-5/69263.html>

<sup>†</sup>ZIB Berlin, Takustr. 7, D-14195 Berlin, Germany (ruprecht@zib.de, schaedle@zib.de, frank.schmidt@zib.de, zschiedrich@zib.de).

The pole condition is similar to Bérenger's perfectly matched layer (PML) method [5], which does not give a representation of the solution in the exterior either. In contrast to the PML method the pole condition method does not rely on a damping of plane waves in the exterior by introducing a complex coordinate stretching. Hence the pole condition method is also applicable to, e.g., drift-diffusion equations.

The exact transparent boundary conditions, which are reviewed briefly in section 2, are nonlocal in time. For a special choice of parameters our approach coincides with the exact transparent boundary conditions. However, one can choose parameters such that the boundary conditions become local in time and space. Local low order approximations of the transparent boundary conditions were derived in the 1970s by Lindman [22] and Engquist and Majda [9]. The use of local high order approximations as considered by Collino [6] was long averted by the difficulties that arise from a stable implementation of high order derivatives at the boundary. Only recently Hagstrom and Warburton [14], Givoli [10], and Givoli and Neta [11] were able, by introducing auxiliary functions, to implement local approximations of arbitrarily high order. Similar to our approach they obtain a system of ODEs, with only local coupling in the spatial discretization. The coefficients  $a_\ell$  of the power series expansion used in the formulation of the pole condition play the role of the auxiliary functions.

In this paper we mainly concentrate on the one-dimensional case. For the simple two-dimensional case of a straight wave guide (i.e., an infinite strip) we will explain shortly how to extend the pole condition approach.

The paper is organized as follows: In section 2 the problem class is introduced and classical transparent boundary conditions are described. Section 3 describes in detail the derivation of the newly developed transparent boundary conditions, which are based on the pole condition. Section 5 describes the spatial discretization and section 6 the time discretization. Finally section 7 gives numerical results for all four equations.

**2. Problem class and classical transparent boundary conditions.** In this section we introduce the problem class. Classical transparent boundary conditions are described and we comment on their implementation very briefly.

For a more detailed discussion on transparent boundary conditions and their approximation, the reader is referred to the excellent reviews by Hagstrom [12, 13], Tsynkov [34], and Givoli [10]. For an overview on transparent boundary conditions for the Schrödinger equation see [2]. The generic equation (1.1) includes the dispersive wave equation (2.1), the drift-diffusion equation (2.2), the heat equation (2.2) with  $d = 0$ , and the Schrödinger equation (2.3). The exact transparent boundary conditions for these equations are well established:

$$(2.1) \quad \partial_{tt}u(t, x) = \partial_{xx}u(t, x) - k^2(t, x)u(t, x) \text{ for } x \in \mathbb{R}, t \geq 0,$$

$$(2.2) \quad \partial_t u(t, x) = \partial_{xx}u(t, x) + 2d\partial_x u(t, x) - k^2(t, x)u(t, x) \text{ for } x \in \mathbb{R}, t \geq 0,$$

$$(2.3) \quad i\partial_t u(t, x) = \partial_{xx}u(t, x) - k^2(t, x)u(t, x) \text{ for } x \in \mathbb{R}, t \geq 0.$$

These equations have to be complemented with appropriate initial conditions.  $k(x, t)$  and  $d$  are assumed to be real. Furthermore  $k(x, t)$  is assumed to be constant outside the space-time strip  $(x, t) \in \Omega_t = [-a, a] \times [0, \infty)$ , and initial values are assumed to be compactly supported in  $[-a, a]$ .

**2.1. Derivation of transparent boundary conditions.** Suppose one is only interested in the solution within the strip  $\Omega_t$  and let  $v$  denote the restriction of  $u$  to

$\Omega_t$ . To obtain an equation for  $v$  boundary conditions along the artificial boundary  $\Gamma_t = \{-a, a\} \times [0, \infty)$  are needed, such that the solution of (1.1) (defined on  $\mathbb{R} \times [0, \infty)$ ) coincides with  $v$  on  $\Omega_t$ . To derive such transparent boundary conditions denote by  $w$  the restriction of  $u$  to the exterior  $\Omega_t^C = \{(-\infty, -a] \cup [a, \infty)\} \times [0, \infty)$ .

A Laplace transformation of  $w$  in  $t$  with dual variable  $\omega$ , where the transformed function is denoted by  $\mathbf{w} = \mathcal{T}(w)$ , i.e.,

$$\mathbf{w}(\omega) = \mathcal{T}(w)(\omega) = \int_0^\infty e^{-\omega t} w(t) dt,$$

yields

$$(2.4) \quad p(\omega) \mathbf{w}(\omega, x) = \partial_{xx} \mathbf{w}(\omega, x) + 2d \partial_x \mathbf{w}(\omega, x) - k^2 \mathbf{w}(\omega, x) \text{ for } |x| > a,$$

$$(2.5) \quad \mathbf{w}(\omega, x) = \mathbf{v}(\omega, x) \text{ for } |x| = a.$$

Equation (2.4) is obtained taking into account that the initial value(s) vanish and  $k$  is constant outside  $\Omega_t$ . The Laplace transform is defined in some right half plane of the complex plane. Assuming that  $\Re(\omega) > 0$  and choosing the branch of the square root such that  $\Re((p(\omega) + d^2 + k^2)^{1/2}) > 0$ , (2.4) has only one bounded solution that solves the problem

$$(2.6) \quad \begin{aligned} \mathbf{w}(\omega, x) &= C_1 e^{(-d - (p(\omega) + k^2 + d^2)^{1/2})x} \text{ for } x > a, \\ \mathbf{w}(\omega, x) &= C_2 e^{(-d + (p(\omega) + k^2 + d^2)^{1/2})x} \text{ for } x < -a. \end{aligned}$$

For the Schrödinger equation we have  $d = 0$ , and thus  $p(\omega)$  has nonnegative imaginary part and so has  $p(\omega) + k^2$ . Hence  $(p(\omega) + k^2)^{1/2}$  takes values in the first quadrant of the complex plane. The solutions given in (2.6) are either decaying exponentially or obey the Sommerfeld radiation condition, i.e., they are outward radiating.

For the drift-diffusion and the heat equation  $p(\omega)$  has nonnegative real part. For all  $d, k \in \mathbb{R}$  it holds that  $-d - (k^2 + d^2)^{1/2} \leq 0$  and  $-d + (k^2 + d^2)^{1/2} \geq 0$ . Thus the real part of  $-d - (p(\omega) + k^2 + d^2)^{1/2}$  is negative and the real part of  $-d + (p(\omega) + k^2 + d^2)^{1/2}$  is positive. The solutions given above are hence decaying exponentially.

As the dispersive wave equation is time reversible, we assume that  $\omega$  is purely imaginary. This formally corresponds to a Fourier transform from  $t = -\infty$  to  $t = \infty$  instead of a Laplace transform along  $[0, \infty)$ . Having  $d = 0$ ,  $(p(\omega) + k^2)^{1/2}$  takes values on the imaginary semiaxis or on an interval on the real line, i.e., in  $\{iy : y \in \mathbb{R}_+\} \cup [0, k]$ . Again, the solutions are either decaying exponentially or obey the Sommerfeld radiation condition.

The constants  $C_1, C_2$  are chosen such that the boundary condition (2.5) is fulfilled. Inserting the normal derivatives  $\partial_\nu v(t, -a) = -\partial_x v(t, -a)$ ,  $\partial_\nu v(t, a) = \partial_x v(t, a)$  into the equation for  $v$ , the solution in the interior is obtained from

$$(2.7) \quad \begin{aligned} p(\partial_t) v(t, x) &= \partial_{xx} v(t, x) + 2d \partial_x v(t, x) - k^2 v(t, x) \text{ for } x \in I, t \geq 0, \\ \partial_\nu v(t, \pm a) &= -\partial_\nu w(t, \pm a) = \mathcal{T}^{-1}((\mp d - (p(\cdot) + k^2 + d^2)^{1/2}) \mathcal{T}(v(\cdot, \pm a)))(t) \\ &= \int_0^t \mathcal{T}^{-1}(\mp d - (p(\cdot) + k^2 + d^2)^{1/2})(t - \tau) v(\tau, \pm a) d\tau. \end{aligned}$$

Alternatively one obtains

$$\begin{aligned}
 p(\partial_t)v(t, x) &= \partial_{xx}v(t, x) + 2d\partial_xv(t, x) - k^2v(t, x) \text{ for } x \in I, t \geq 0, \\
 (2.8) \quad v(t, \pm a) &= \mathcal{T}^{-1}\left(\left(\mp d - (p(\cdot) + k^2 + d^2)^{1/2}\right)^{-1}\mathcal{T}(\partial_\nu v(\cdot, \pm a))\right)(t) \\
 &= \int_0^t \mathcal{T}^{-1}\left(\left(\mp d - (p(\cdot) + k^2 + d^2)^{1/2}\right)^{-1}\right)(t - \tau)\partial_\nu v(\tau, \pm a)d\tau.
 \end{aligned}$$

As is seen from (2.7) and (2.8) transparent boundary conditions are in general of convolution type. The discretization of (2.8) with respect to time is not straightforward and may introduce instabilities. A stable discretization is obtained using convolution quadrature [24, 25], based on the same time integration scheme as used in the interior. It is shown in [28] that this is equivalent to the derivation of time-discrete transparent boundary conditions given below.

**2.2. Derivation of time-discrete transparent boundary conditions.** The equation for  $u$  (1.1) is discretized in time using an A-stable multistep method, such as the trapezoidal rule. Time-discrete transparent boundary conditions are now derived following almost the same procedure as above. The only difference is that instead of applying a Laplace transform in the variable  $t$ , a  $Z$ -transform is applied.

$$\mathbf{u}(\zeta) := \mathcal{Z}(u)(\zeta) := \sum_n u(nh)\zeta^n.$$

Denoting by  $\delta(\zeta)$ <sup>1</sup> the generating function of the multistep method, the time-discrete transparent boundary condition is

$$(2.9) \quad v(nh, \pm a) = \mathcal{Z}^{-1}\left(\mp d - (p(\delta(\cdot)/h) + k^2 + d^2)^{-1/2}\mathcal{Z}(\partial_\nu v)(\cdot)\right)(n) = \sum_{j=0}^n \kappa_{n-j}\partial_\nu v_j,$$

where the convolution weights  $\kappa_n$  are given by the power series expansion

$$(2.10) \quad \mp d - (p(\delta(\zeta)/h) + k^2 + d^2)^{-1/2} = \sum_j \kappa_j \zeta^j.$$

In general the weights have to be calculated numerically. To calculate  $N$  weights with precision  $\varepsilon$  the complexity is  $\mathcal{O}(N \log N \varepsilon \log(\varepsilon))$ ; cf. [25, sec. 7]. In our simple setting it should, however, be possible for the trapezoidal rule to calculate the weights analytically; see, e.g., [3, 32, 1]. The computational effort for the naive direct evaluation of the convolution (2.10) requires  $\mathcal{O}(N^2)$  operations and  $\mathcal{O}(N)$  memory (direct convolution). Using an algorithm developed in [17] the operation count could be reduced to  $\mathcal{O}(N \log(N)^2)$ . For the evaluation of the convolution a fast oblivious algorithm is at hand [27, 23] that evaluates (2.9) for  $n = 1, \dots, N$  with precision  $\varepsilon$  using  $\mathcal{O}(N \log(N) \log(1/\varepsilon))$  operations and  $\mathcal{O}(\log(N) \log(1/\varepsilon))$  memory (fast, oblivious convolution). In section 7.1.1 the newly developed pole condition is compared with

<sup>1</sup>In case of the trapezoidal rule  $\delta(\zeta) = 2\frac{1+\zeta}{1-\zeta}$ . For the implicit Euler method  $\delta(\zeta) = \frac{1}{1-\zeta}$ . In general  $\delta$  is the quotient of the generating polynomials of the multistep method [15, Chap. III, sec. 2]. An extension to Runge–Kutta methods is possible [26].

the direct convolution, the fast and oblivious convolution, an algorithm using a Padé approximation of the convolution kernel [20, 33, 2], and an adaptive PML [2].

In the derivation of the exact transparent boundary conditions in sections 2.1 and 2.2 it was *necessary* after applying a Laplace or  $Z$ -transform to solve the second order differential equation in  $x$ , and to choose among two linear independent solutions the one that has the correct asymptotic behavior for  $x \rightarrow \infty$ . For higher spatial dimensions, however, this is possible only in very special cases, if at all. In what follows we present a more general concept that avoids solving ODEs and picking certain solutions. The basis for this is the pole condition approach proposed by Schmidt in [30, 19, 31].

**3. An alternative derivation of transparent boundary conditions.** The basic idea of the pole condition is to test the exterior solution against any incoming field  $\exp(sx)$  by trying to evaluate  $\int_a^\infty u(x) \exp(-s(x-a)) dx$ . This integral will diverge in case  $u(x)$  has incoming components. What is incoming and outgoing is determined by the phase of the test function  $\exp(sx)$ , i.e., by the complex value  $s$ . The situation will be analyzed for each type of equation in section 3.2.

**3.1. Variational formulation.** The starting point is the Laplace transform in  $t$  of (1.1),

$$(3.1) \quad p(\omega) \mathbf{u}(\omega, x) = \partial_{xx} \mathbf{u}(\omega, x) + 2d \partial_x \mathbf{u}(\omega, x) - K(\mathbf{u}).$$

Here the term  $K(\mathbf{u})$  is the Laplace transform of  $k^2(x, t)u(x, t)$  and additionally includes the initial value(s). Multiplying by a test function  $v$  and integrating over  $\mathbb{R}$  the variational form is given as follows: Find  $\mathbf{u} \in H^1(\mathbb{R})$  such that

$$(3.2) \quad \int_{\mathbb{R}} p(\omega) \mathbf{u}(\omega, x) v(x) dx = \int_{\mathbb{R}} -\partial_x \mathbf{u}(\omega, x) \partial_x v(x) + 2d \partial_x \mathbf{u}(\omega, x) v(x) - K(\mathbf{u}) v(x) dx$$

for all  $v \in H^1(\mathbb{R})$ .  $\omega$  may be considered to be the dual variable with respect to  $t$  or the generating function  $\delta(\zeta)$ . It is sufficient to test against all  $v$  in some dense subset, and we will use that freedom and restrict ourselves to the set of all  $v \in H^1(\mathbb{R})$ , such that  $v(x) = ce^{-s(x-a)}$  for  $x > a$  and  $v(x) = ce^{s(x+a)}$  for  $x < -a$ , with  $\Re s > 0$  and  $c \in \mathbb{C}$ . We do not have a proof that the set of exponential test functions is dense in  $H^1(\mathbb{R})$ . The motivation for choosing these exponentials is, however, different. If a solution in the right exterior has an incoming part, then the result after testing against  $e^{s(x+a)}$  will explode for some  $s$  in the region of the complex plane that corresponds to incoming solutions. Splitting the integral in (3.2) one obtains

$$(3.3) \quad \begin{aligned} & \int_{[-a, a]} p(\omega) \mathbf{u}(\omega, x) v(x) dx + \int_{|x| > a} p(\omega) \mathbf{u}(\omega, x) v(x) dx \\ &= \int_{[-a, a]} -\partial_x \mathbf{u}(\omega, x) \partial_x v(x) + 2d \partial_x \mathbf{u}(\omega, x) v(x) - K(\mathbf{u}) v(x) dx \\ & \quad + \int_{|x| > a} -\partial_x \mathbf{u}(\omega, x) \partial_x v(x) + 2d \partial_x \mathbf{u}(\omega, x) v(x) - k^2 \mathbf{u}(\omega, x) v(x) dx. \end{aligned}$$

Inserting the special form of  $v$  outside  $[-a, a]$  and setting  $c = 1$  one obtains

$$\begin{aligned}
 (3.4) \quad & \int_{[-a, a]} p(\omega) \mathbf{u}(\omega, x) v(x) dx + p(\omega) U^{(l)}(\omega, s) + p(\omega) U^{(r)}(\omega, s) \\
 &= \int_{[-a, a]} -\partial_x \mathbf{u}(\omega, x) \partial_x v(x) + 2d \partial_x \mathbf{u}(\omega, x) v(x) - K(\mathbf{u}) v(x) dx \\
 &\quad + s(sU^{(l)}(\omega, s) - \mathbf{u}(\omega, -a)) - 2d(sU^{(l)}(\omega, s) - \mathbf{u}(\omega, -a)) - k^2 U^{(l)}(\omega, s) \\
 &\quad + s(sU^{(r)}(\omega, s) - \mathbf{u}(\omega, a)) + 2d(sU^{(r)}(\omega, s) - \mathbf{u}(\omega, a)) - k^2 U^{(r)}(\omega, s),
 \end{aligned}$$

where

$$U^{(r)}(\omega, s) = \int_a^\infty \mathbf{u}(\omega, x) e^{-s(x-a)} dx = \int_0^\infty \mathbf{u}(\omega, x+a) e^{-sx} dx$$

and

$$U^{(l)}(\omega, s) = \int_{-\infty}^{-a} \mathbf{u}(\omega, x) e^{s(x+a)} dx = \int_0^\infty \mathbf{u}(\omega, -x-a) e^{-sx} dx$$

are the Laplace transforms of the solution in the exterior. Transparent boundary conditions are now set by imposing appropriate conditions on  $U^{(l,r)}$ ; cf. section 3.2.

Classical transparent boundary conditions are connecting Neumann and Dirichlet data at the boundary. The following reinterpretation of (3.4) will supply the Neumann data at the boundary. Suppose a function  $u$  on  $I = [-a, a]$  is given obeying (3.1). Multiplying by a test function and integrating by parts yields

$$\begin{aligned}
 \int_I p(\omega) \mathbf{u}(\omega, x) v(x) dx &= \int_I -\partial_x \mathbf{u}(\omega, x) \partial_x v(x) dx + 2d \partial_x \mathbf{u}(\omega, x) v(x) - K(\mathbf{u}) v(x) dx \\
 &\quad + \partial_x \mathbf{u}(\omega, a) v(a) - \partial_x \mathbf{u}(\omega, -a) v(-a).
 \end{aligned}$$

Choosing a test function that vanishes at  $-a$  and is 1 at  $a$ , the above equation allows us to weakly define the outward normal derivative of  $\mathbf{u}(\omega, a)$  at  $x = a$  by

$$\partial_x \mathbf{u}(\omega, a) v(a) = \int_I p(\omega) \mathbf{u}(\omega, x) v + \partial_x \mathbf{u}(\omega, x) \partial_x v - 2d \partial_x \mathbf{u}(\omega, x) v + K(\mathbf{u}) v dx.$$

Similarly for the outward normal derivative of  $\mathbf{u}(\omega, -a)$  at  $x = -a$  one obtains

$$-\partial_x \mathbf{u}(\omega, -a) v(-a) = \int_I p(\omega) \mathbf{u}(\omega, x) v + \partial_x \mathbf{u}(\omega, x) \partial_x v - 2d \partial_x \mathbf{u}(\omega, x) v + K(\mathbf{u}) v dx.$$

**3.2. Pole condition.** Suppose that  $U$ , the Laplace transform in the exterior, as a function of  $s$  has some singularities in the complex plane. By Cauchy's integral formula

$$U(s) = \frac{1}{2\pi i} \int_\gamma (s - \tau)^{-1} U(\tau) d\tau,$$

where  $\gamma$  is a path enclosing the singularities of  $U$ . This path integral may be interpreted as a superposition of  $(s - \tau)^{-1}$ , as is easily seen by inserting the Riemann sum for the path integral, which gives

$$U(s) = \lim_{N \rightarrow \infty} \sum_{j=1}^N b_j(N, U(\tau_j)) \frac{1}{s - \tau_j}$$

for certain weights  $b_j$ . Transforming back to space domain we have the correspondence

$$\frac{1}{s - \tau} \leftrightarrow e^{x\tau}.$$

Depending on the location of  $\tau$  in the complex plane,  $e^{x\tau}$  is outward radiating/exponentially decreasing or incoming/exponentially increasing. This way the complex plane can be divided into two regions; a region  $\mathbb{C}^{\text{in}} = \{\tau \in \mathbb{C} : e^{x\tau} \text{ is incoming} \}$  and a region  $\mathbb{C}^{\text{out}} = \{\tau \in \mathbb{C} : e^{x\tau} \text{ is outward radiating} \}$ . Now split the contour  $\gamma$  into two contours  $\gamma_{\text{in}}$  and  $\gamma_{\text{out}}$ , where  $\gamma_{\text{in}}$  lies in  $\mathbb{C}^{\text{in}}$  and encloses all singularities of  $U$  in this region, while  $\gamma_{\text{out}}$  lies in  $\mathbb{C}^{\text{out}}$  enclosing all singularities in that region. The integral over  $\gamma$  is then decomposed as follows:

$$U(s) = \int_{\gamma_{\text{in}}} (s - \tau)^{-1} U(\tau) d\tau + \int_{\gamma_{\text{out}}} (s - \tau)^{-1} U(\tau) d\tau.$$

Requiring that  $\mathbf{u}(\omega, x)$  is purely outward radiating is now equivalent to the condition that  $\int_{\gamma_{\text{in}}} (s - \tau)^{-1} U(\tau) d\tau = 0$ , which in turn is equivalent to the condition that  $U(s)$  is analytic in  $\mathbb{C}^{\text{in}}$ . Such a splitting is always possible in case incoming and outgoing solutions are different, i.e., the problem is not degenerated. In the degenerate case the singularities corresponding to incoming and outgoing solutions coincide. We can summarize this in the following definition.

**DEFINITION 3.1** (pole condition). *A solution  $\mathbf{u}(\omega, x)$  obeys the pole condition if the Laplace transform  $U(\omega, s)$  is analytic in  $\mathbb{C}^{\text{in}}$ .*

The equivalence of the pole condition with the Sommerfeld radiation condition for the two-dimensional Helmholtz equation for a homogeneous exterior domain was proven in [19]. What these regions  $\mathbb{C}^{\text{out}}$  and  $\mathbb{C}^{\text{in}}$  look like is discussed in sections 3.2.1 to 3.2.4 for the different types of equations.

The above reasoning can be made more explicit for the simple one-dimensional model problem. It is stressed, however, that for the construction of the transparent boundary condition the following explicit calculations are not necessary. They are presented here to give the reader some confidence in the method and to show how classical transparent boundary conditions are contained as a special case.

Suppose for the moment that  $\mathbf{u}$  is given on  $[-a, a]$  and consider the right exterior only. The equation for  $U^{(r)}$  is then

$$-p(\omega)U^{(r)}(\omega, s) + s^2U^{(r)}(\omega, s) + 2dsU^{(r)}(\omega, s) - k^2U^{(r)}(\omega, s) = r(s, \mathbf{u})$$

with the remainder term

$$r(s, \mathbf{u}) = \partial_x \mathbf{u}(\omega, a)v(a) + 2d\mathbf{u}(\omega, a) + s\mathbf{u}(\omega, a),$$

which is analytic in  $s$ . Solving for  $U^{(r)}$  we obtain

$$(3.5) \quad U^{(r)}(\omega, s) = (s^2 + 2ds - (p(\omega) + k^2))^{-1} r(s, \mathbf{u}).$$

For fixed  $\omega$  there are always two roots  $s^{(-)}$  and  $s^{(+)}$  of  $s^2 + 2ds - (p(\omega) + k^2)$ , such that  $U$  can be decomposed as follows:

$$(3.6) \quad U^{(r)}(\omega, s) = (s - s^{(+)})^{-1} r_1(\omega, \mathbf{u}) + (s - s^{(-)})^{-1} r_2(\omega, \mathbf{u}),$$

with

$$r_1(\omega, \mathbf{u}) = \frac{1}{2} \left( \mathbf{u}(\omega, a) + \frac{\partial_x \mathbf{u}(\omega, a)v(a) + 2d\mathbf{u}(\omega, a)}{\sqrt{p(\omega) + k^2 + d^2}} \right)$$

and

$$r_2(\omega, \mathbf{u}) = \frac{1}{2} \left( \mathbf{u}(\omega, a) - \frac{\partial_x \mathbf{u}(\omega, a)v(a) + 2d\mathbf{u}(\omega, a)}{\sqrt{p(\omega) + k^2 + d^2}} \right).$$

Transforming back to space domain, the summands in (3.6) correspond to solutions  $\exp(xs^{(+)})$  and  $\exp(xs^{(-)})$ . Depending on the location of  $s^{(\pm)}$  in the complex plane incoming and outgoing, exponentially decaying, and exponentially increasing solutions can be identified. A similar splitting is obtained for the left boundary.

The possible location of the poles  $s^{(+)}$  and  $s^{(-)}$  for the four different equations is considered more closely in sections 3.2.1 to 3.2.4. It is then argued how to construct boundary conditions that in the case of the Schrödinger and wave equations distinguish incoming and outgoing waves. In case of the heat and drift-diffusion equations the boundary condition distinguishes between bounded (physically reasonable) and unbounded (unphysical) solutions.

**3.2.1. Heat equation.** Here  $p(\omega) = \omega$ , where  $\omega$  takes values in the right half plane. Hence  $p(\omega) + k^2$  is the right half plane shifted to the right by  $k^2$ . The roots of  $s^2 - (p(\omega) + k^2)$  take values in regions to the left and right of the imaginary axis that are bounded by hyperbolas, as sketched in the right plot in Figure 3.1. Clearly the roots to the right correspond to unphysical exponentially increasing solutions. To exclude these, one requires that  $U(\omega, s)$  is analytic in the right half plane.

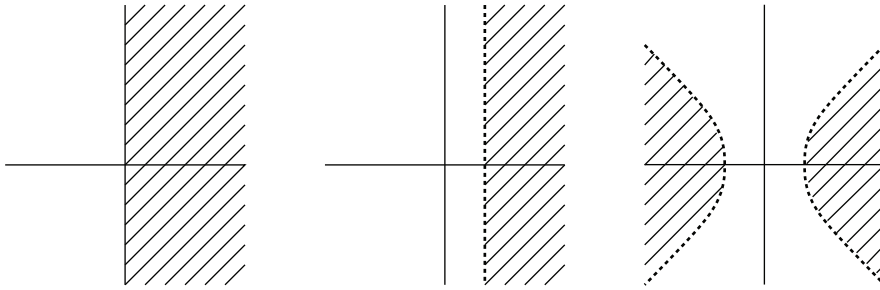


FIG. 3.1. *Left: possible values of  $p(\omega)$ . Middle: possible values of  $p(\omega) + k^2$ . Right: location of the roots  $s^{(\pm)}$ . To each root in the left region there corresponds one root in the right region.*

**3.2.2. Schrödinger equation.** In this case  $p(\omega) = i\omega$ , where  $\omega$  takes values in the right half plane. Hence  $p(\omega) + k^2$  is the upper half plane—the right half plane rotated counterclockwise by  $\pi/4$  and shifted by  $k^2$ —as sketched in the middle plot of Figure 3.2. The roots of  $s^2 - (p(\omega) + k^2)$  take values in the first and third quadrants, as sketched in the right plot in Figure 3.2. The roots in the first quadrant correspond to unphysical solutions that either are exponentially increasing or have the wrong phase shift. To exclude these one may for instance require that  $U(\omega, s)$  is analytic in the upper right half plane above the bisecting line of the second and fourth quadrants.

**3.2.3. Wave equation.** If  $p(\omega) = \omega^2$ ,  $p(\omega) + k^2$  takes values everywhere. The imaginary axis is mapped to the axis  $\{\Im s = 0; \Re s < k^2\}$ . The roots now fill the whole complex plane. The values along the cross as indicated in the right plot of Figure 3.3 correspond to the axis  $\{\Im s = 0; \Re s < k^2\}$ . Solutions corresponding to roots in the lower half plane are incoming; transformed back to space domain they do not satisfy the Sommerfeld radiation condition.



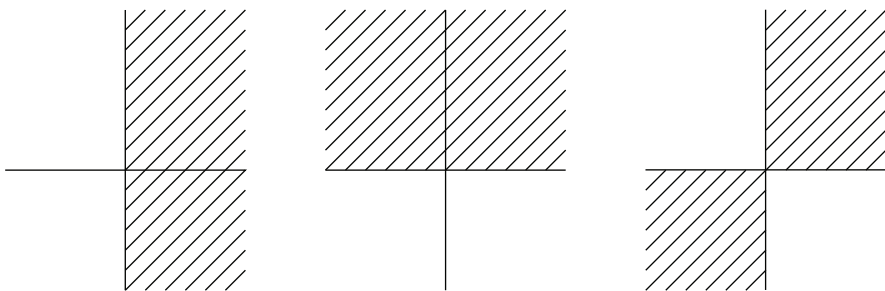


FIG. 3.2. Left: possible values of  $p(\omega)$ . Middle: possible values of  $p(\omega) + k^2$ . Right: location of the roots  $s^{(\pm)}$ . To each root in the first quadrant there corresponds one root in the third quadrant.

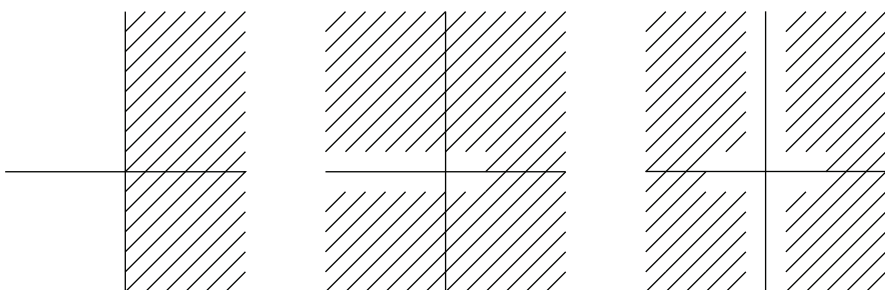


FIG. 3.3. Left: possible values of  $p(\omega)$ . Middle: possible values of  $p(\omega) + k^2$ . Right: location of the roots  $s^{(\pm)}$ .

**3.2.4. Drift-diffusion equation.** If  $p(\omega) = \omega$ , where  $\omega$  takes values in the right half plane, then  $p(\omega) + k^2$  is shifted by  $k^2$ . The roots of  $s^2 + 2ds - (p(\omega) + k^2)$  take values in regions to the left and right of the imaginary axis that are bounded by hyperbolas, as sketched in the right plot in Figure 3.4. Clearly the roots to the right correspond to unphysical exponentially increasing solutions. In the drift-diffusion example the position of the roots is different for the left and right boundaries; they are symmetric with respect to the  $\Re s = \pm d$  for the left and right boundaries, respectively. To exclude the roots in the right region one requires that  $U(\omega, s)$  be analytic in the right half plane, bounded by the axis  $\Re s = \pm d$ .

Calculating the roots  $s^{(\pm)}$  and the functions  $r_1$  and  $r_2$  for each of the above cases

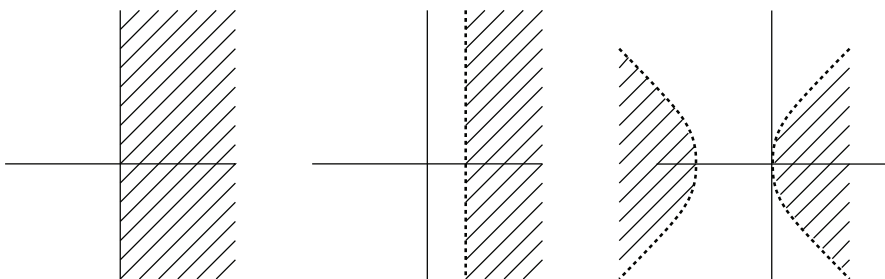


FIG. 3.4. Left: possible values of  $p(\omega)$ . Middle: possible values of  $p(\omega) + k^2$ . Right: location of the roots  $s^{(\pm)}$ . To each root in the left region there corresponds one root in the right region.

one obtains

$$\mathbf{u}(\omega, a) + \frac{\partial_\nu \mathbf{u}(\omega, a)v(a)}{\pm d + \sqrt{p(\omega) + k^2 + d^2}} = 0$$

and

$$(\pm d + \sqrt{p(\omega) + k^2 + d^2})\mathbf{u}(\omega, 0) + \partial_\nu \mathbf{u}(\omega, a)v(a) = 0,$$

which is equivalent to the boundary conditions given in (2.8), (2.9), and (2.7).

**3.3. The pole condition in Hardy space.** We will now reformulate the boundary condition in a way that will allow an easy implementation. For this we map the domain where  $U(s)$  is required to be analytic to the unit disc. With this change of coordinates, the condition on  $U$  to be analytic in some half plane is now formulated as the condition on  $U$  to be analytic on the unit disk. In the new coordinate  $U$  may then be expanded into a power series.

The mapping is done by a Möbius transformation, which is given by

$$(3.7) \quad \Phi : s \mapsto \tilde{s} = \frac{\alpha s + \beta}{\gamma s + \delta}.$$

In case of the heat, wave, and Schrödinger equations we set  $\alpha = \gamma = 1$ ,  $\beta = s_0(\omega)$ , and  $\delta = -s_0(\omega)$ , such that the Möbius transform maps the half plane

$$(3.8) \quad \{z : \Re(-z/s_0(\omega)) \leq 0\}$$

onto the unit disk. The point  $-s_0(\omega)$  is mapped to 0 and the infinite point is mapped to 1. In this case the inverse transform is given by

$$(3.9) \quad \Phi^{-1} : \tilde{s} \mapsto s = s_0(\omega) \frac{\tilde{s} + 1}{\tilde{s} - 1}.$$

Using a result on Laplace transforms (see, e.g., [7, Theorem 33.4]), it holds true that

$$\lim_{s \rightarrow \infty} sU^{(r)}(s) = \mathbf{u}(\omega, a) \quad \text{and} \quad \lim_{s \rightarrow \infty} sU^{(l)}(s) = \mathbf{u}(\omega, -a).$$

In particular for large arguments  $U^{(l,r)}(s)$  is proportional to  $1/s$ . As the Möbius transform maps  $s = \infty$  to  $\tilde{s} = 1$ , this justifies the following ansatz:

$$(3.10) \quad \tilde{U}^{(r,l)}(\omega, \tilde{s}) := U^{(r,l)}(\omega, \Phi^{-1}(\tilde{s})) = (\tilde{s} - 1) \sum_{\ell=0}^{\infty} a_\ell(\omega) \tilde{s}^\ell.$$

Taking into account the values of the limit, another possible choice would have been

$$(3.11) \quad \tilde{U}^{(r,l)}(\omega, \tilde{s}) := U^{(r,l)}(\omega, \Phi^{-1}(\tilde{s})) = (\tilde{s} - 1) \left( \frac{\mathbf{u}(\omega, \pm a)}{2s_0} + (\tilde{s} - 1) \sum_{\ell=0}^{\infty} a_\ell(\omega) \tilde{s}^\ell \right).$$

Using (3.11) would be equivalent (up to a scaling of the  $a_\ell$ ) to the discretization used in [18]. However, we opt for (3.10), as we want to avoid dividing by  $s_0$ . The reason is that for the wave equation we will choose  $s_0$  to be a time derivative. Hence a multiplication by  $1/s_0$  would result in an integral operator. By introducing the time

integral over the Dirichlet boundary values as an auxiliary variable, the discretization of the integral operator can be done local in time. The ansatz

$$\tilde{U}^{(r,l)}(\omega, \tilde{s}) := U^{(r,l)}(\omega, \Phi^{-1}(\tilde{s})) = \sum_{\ell=0}^{\infty} a_{\ell}(\omega) \tilde{s}^{\ell},$$

which we used in [29], would lead to a singular mass matrix  $M$  in (5.14).

In the following we drop the tilde and the superscript  $r, l$  on the  $U$  and write  $U(\tilde{s})$  for  $\tilde{U}(\tilde{s})$ .

In case of the drift-diffusion equation the two regions with the poles are symmetric with respect to the axis parallel to the imaginary axis shifted by  $\pm d$  for the right and left boundaries, respectively. Thus different Möbius transforms are used for the left and right boundaries. For the right boundary we set  $a^{(r)} = (d - s0)$ ,  $b^{(r)} = -(d + s0)$ ,  $c^{(r)} = -1$ ,  $d^{(r)} = 1$  and for the left boundary we set  $a^{(l)} = (-d - s0)$ ,  $b^{(l)} = -(-d + s0)$ ,  $c^{(l)} = -1$ ,  $d^{(l)} = 1$ .

The space of functions  $f$  that are analytic in the unit disk, such that the integral means

$$\int_0^{2\pi} |f(re^{i\theta})|^2 d\theta$$

are bounded as  $r \rightarrow 1$ , is called the *Hardy space*  $H^2$ ; cf. [8]. The Hardy space can be characterized as the space of functions  $f(z) = \sum_{\ell=0}^{\infty} a_{\ell} z^{\ell}$  such that  $\sum_{\ell=0}^{\infty} |a_{\ell}|^2$  is finite [21, Chap. III, sec. 3.4].

**4. Extension to two-dimensional waveguide geometries.** Consider the following simple waveguide problem in two space dimensions. The unknown function  $u$  takes values in  $\mathbb{C}$  and is a solution of

$$\begin{aligned} (4.1) \quad & p(\partial_t)u(t, x, y) = \partial_{xx}u(t, x, y) + \partial_{yy}u(t, x, y) + 2d\partial_xu(t, x, y) - k^2(t, x, y)u(t, x, y) \\ & \text{for } (x, y) \in \mathbb{R} \times [-b, b], \quad t \geq 0, \\ & B(u(t, x, \pm b)) = 0 \quad \text{for } x \in \mathbb{R}, \quad t \geq 0. \end{aligned}$$

Here  $k$  is a real-valued, sufficiently smooth function. Rewriting this for a vector-valued function  $\mathbf{u}(t, x) = u(t, x, \cdot)$  one obtains

$$(4.2) \quad p(\partial_t)\mathbf{u}(t, x) = \partial_{xx}\mathbf{u}(t, x) + 2d\partial_x\mathbf{u}(t, x) - K(t, x)\mathbf{u}(t, x) \quad \text{for } x \in \mathbb{R}, \quad t \geq 0,$$

where  $K(t, x) = -\partial_{yy} + M_{k^2}$  is a linear operator  $\mathbf{u} \mapsto K(t, x)u(y) = -\partial_{yy}u(y) + k^2(t, x, y)u(y)$ . For an appropriate boundary condition, e.g., periodic boundary conditions, i.e.,  $B(u(t, x, \pm b)) = u(t, x, b) - u(t, x, -b)$ , the positivity of  $K$  guarantees that the derivation of transparent boundary conditions given in section 3 remains valid, except for the explicit decomposition (3.6).

**5. Space discretization.** Space discretization is done using finite elements in the interior. The situation for the one-dimensional problem is described in some detail. The space discretization for a two-dimensional waveguide problem is done using the tensor product structure of a Cartesian mesh.

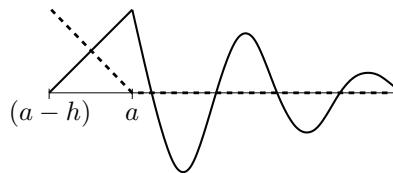


FIG. 5.1. Boundary exp-element for  $p = 1$  with the two test functions, shown as dashed and solid lines.

**5.1. One-dimensional case.** Ansatz and test functions are globally continuous functions, which are piecewise polynomials. Choosing ansatz and test functions which are supported by only one single or two neighboring finite elements yields the well-established sparse mass matrix  $M$  and a system matrix  $S$ . Locally on an interval  $I$  (finite element) of length  $h$  for first order linear ansatz and test functions one obtains

$$M^{loc} = \frac{h}{6} \begin{pmatrix} 2 & 1 \\ 1 & 2 \end{pmatrix}, \quad S^{loc} = \frac{1}{h} \begin{pmatrix} -1 & 1 \\ 1 & -1 \end{pmatrix} + 2d \frac{1}{2} \begin{pmatrix} -1 & 1 \\ -1 & 1 \end{pmatrix} - k^2 \frac{h}{6} \begin{pmatrix} 2 & 1 \\ 1 & 2 \end{pmatrix}.$$

In the numerical experiments, finite elements up to polynomial degree  $p = 4$  are used. Thus for the  $p + 1$  ansatz functions  $\{\phi_i\}$ ,  $i = 1, \dots, p + 1$ , the local  $(p + 1) \times (p + 1)$  matrices are

$$M_{i,j}^{loc} = \int_I \phi_j \phi_i dx, \quad S_{i,j}^{loc} = \int_I \partial_x \phi_j \partial_x \phi_i + 2d \partial_x \phi_j \phi_i - k^2 \phi_j \phi_i dx.$$

These local matrices have to be assembled to the global matrices  $M$  and  $S$ . In sloppy notation (neglecting boundary terms) one obtains, collecting degrees of freedom into a vector  $\tilde{\mathbf{u}}$ ,

$$(5.1) \quad p(\omega) \tilde{M} \tilde{\mathbf{u}}(\omega) = \tilde{S} \tilde{\mathbf{u}}(\omega).$$

The situation at the boundary is different. The test function  $v_s(x)$ , which is depicted in Figure 5.1 for the right artificial boundary point for fixed  $s$ , is given by

$$v_s(x) = \begin{cases} e^{-s(x-a)}, & x \geq a, \\ \frac{x-(a-h)}{h}, & a-h \leq x \leq a. \end{cases}$$

Here  $v_s(x)$  is not one function but a family of functions parameterized by  $s \in \mathbb{C}^+$ .  $v_s(x)$  is globally continuous but is not finitely supported (it is supported by  $[a-h, \infty)$ ). Assuming that  $\mathbf{u}(\omega, x)$  on  $[(a-h), a]$  is given as the superposition  $\sum_{j=1}^{p+1} u_j(\omega) \phi_j(x)$  of  $\phi_j(x)$ , the equation obtained by testing against  $v_s(x)$  is

$$(5.2) \quad \int_{[a-h, a]} p(\omega) \sum_{j=1}^{p+1} u_j(\omega) \phi_j(x) \frac{x-(a-h)}{h} dx + p(\omega) U(\omega, s) \\ = \int_{[a-h, a]} \sum_{j=1}^{p+1} u_j(\omega) \left( -\phi_j'(x) \frac{1}{h} + 2d \phi_j'(x) \frac{x-(a-h)}{h} - k^2 \phi_j(x) \frac{x-(a-h)}{h} \right) dx \\ + s(sU(\omega, s) - \mathbf{u}(\omega, a)) + 2d(sU(\omega, s) - \mathbf{u}(\omega, a)) - k^2 U(\omega, s).$$

For the Laplace transform  $U(\omega, s)$  of the solution  $\hat{u}(\omega, x)$  in the right exterior domain the series expansion (3.10) with coefficients  $a_\ell(\omega)$  is inserted, and the series is truncated by setting  $a_\ell = 0$  for  $\ell \geq L + 1$ . In what follows equations for the unknown coefficients  $a_\ell(\omega)$  are derived. The two cases  $d = 0$  and  $d \neq 0$  are treated separately.

Case  $d = 0$ . Setting

$$\hat{u}^{(0)}(a) = \sum_{j=1}^{p+1} \int_{[a-h, a]} u_j(\omega) \phi_j(x) \frac{x - (a - h)}{h} dx$$

and

$$\hat{u}^{(2)}(a) = \sum_{j=1}^{p+1} \int_{[a-h, a]} -u_j(\omega) \phi_j'(x) \frac{1}{h} dx$$

the weak form of the Neumann data can be evaluated as

$$(5.3) \quad \hat{u}'(a) = (p + k^2) \hat{u}^{(0)}(a) - \hat{u}^{(2)}(a).$$

Here it is assumed without loss of generality that the initial value(s) are supported in  $[-a + h, a - h]$  and that  $k$  is constant outside  $[-a + h, a - h]$ . With these settings (5.2) in the variable  $\tilde{s}$  may be conveniently written as

$$(5.4) \quad \begin{aligned} & p(\omega) (\hat{u}^{(0)}(a) + U^{(r)}(\omega, \tilde{s})) \\ &= \hat{u}^{(2)}(a) + s_0(\omega) \frac{\tilde{s} + 1}{\tilde{s} - 1} \left( s_0(\omega) \frac{\tilde{s} + 1}{\tilde{s} - 1} U^{(r)}(\omega, \tilde{s}) - \mathbf{u}(\omega, a) \right) \\ & \quad - k^2 (\hat{u}^{(0)}(a) + U^{(r)}(\omega, \tilde{s})). \end{aligned}$$

Inserting the series representation (3.10), multiplying by  $(\tilde{s} - 1)$ , and rearranging terms yields

$$\begin{aligned} & p(\omega) \left( (\tilde{s} - 1) \hat{u}^{(0)}(a) + (\tilde{s} - 1)^2 \sum_{\ell=0}^{\infty} a_\ell(\omega) \tilde{s}^\ell \right) \\ &= (\tilde{s} - 1) \hat{u}^{(2)}(a) + s_0^2(\tilde{s} + 1)^2 \sum_{\ell=0}^{\infty} a_\ell(\omega) \tilde{s}^\ell - s_0(\tilde{s} + 1) \mathbf{u}(\omega, a) \\ & \quad - k^2 \left( (\tilde{s} - 1) \hat{u}^{(0)}(a) + (\tilde{s} - 1)^2 \sum_{\ell=0}^{\infty} a_\ell(\omega) \tilde{s}^\ell \right). \end{aligned}$$

Comparing coefficients, one obtains

$$(5.5) \quad p(\omega) (-\hat{u}^{(0)}(a) + a_0) = -\hat{u}^{(2)}(a) + s_0^2 a_0 - s_0 \mathbf{u}(\omega, a) - k^2 (-\hat{u}^{(0)}(a) + a_0),$$

$$(5.6) \quad \begin{aligned} p(\omega) (\hat{u}^{(0)}(a) - 2a_0 + a_1) &= \hat{u}^{(2)}(a) + s_0^2(2a_0 + a_1) \\ & \quad - s_0 \mathbf{u}(\omega, a) - k^2 (\hat{u}^{(0)}(a) - 2a_0 + a_1), \end{aligned}$$

$$(5.7) \quad p(\omega) (a_{\ell-1} - 2a_\ell + a_{\ell+1}) = s_0^2(a_{\ell-1} + 2a_\ell + a_{\ell+1}) - k^2(a_{\ell-1} - 2a_\ell + a_{\ell+1}).$$

These equations hold for the right boundary at  $x = a$ , with the Laplace transform taken from the boundary to  $\infty$ . With the corresponding definition of  $\hat{u}^{(0)}(-a)$  and

$\hat{u}^{(2)}(-a)$  we can also define  $\hat{u}'(-a)$  and get identical equations for the left boundary at  $x = -a$  by using a series expansion for  $U^{(l)}(\omega, \tilde{s})$ .

Let us have a closer look at (5.5). So far we did not specify  $s_0$ . If we would choose  $s_0(\omega)$  such that  $s_0(\omega) = -\sqrt{k^2 + p(\omega)}$ , i.e.,  $s_0^2(\omega) - p(\omega) - k^2 = 0$ , then by using (5.3), equation (5.5) reduces to

$$(5.8) \quad \hat{u}'(a) = -\sqrt{k^2 + p(\omega)} \mathbf{u}(\omega, a) \Leftrightarrow -\frac{1}{\sqrt{k^2 + p(\omega)}} \hat{u}'(a) = \mathbf{u}(\omega, a),$$

which is equivalent to the exact transparent boundary condition (2.8) or (2.9). In this case the equations for the  $a_\ell$  are decoupled. Thus by construction we have the following theorem.

**THEOREM 5.1.** *For the choice  $s_0(\omega) = -\sqrt{p(\omega) + k^2}$  the pole condition-based transparent boundary condition coincides with the classical transparent boundary condition, respectively, the time-discrete transparent boundary condition.*

Given the Dirichlet data, one might use (5.6) and (5.7) to solve for the auxiliary unknowns  $a_\ell$ . If  $a_0$  is inserted into (5.5), then this equation connects Dirichlet data and weak Neumann data and may thus be interpreted as a classical transparent boundary condition.

*Case  $d \neq 0$ .* Setting additionally

$$\hat{u}^{(1)}(a) = \sum_{j=1}^{p+1} \int_{[a-h, a]} u_j(\omega) \phi_j'(x) \frac{x - (a-h)}{h} dx$$

the Neumann data is now given by

$$(5.9) \quad \hat{u}'(a) = p(\omega) \hat{u}^{(0)}(a) - \hat{u}^{(2)}(a) - 2d\hat{u}^{(1)}(a) + k^2 \hat{u}^{(0)}(a).$$

Equation (5.2) in the variable  $\tilde{s}$  is conveniently written as

$$(5.10) \quad \begin{aligned} p(\omega) \hat{u}^{(0)}(\omega) + p(\omega) U^{(r)}(\omega, \tilde{s}) &= \hat{u}^{(2)} + 2d\hat{u}^{(1)} - k^2 \hat{u}^{(0)} \\ &+ \frac{(s_0 - d)\tilde{s} + (d + s_0)}{\tilde{s} - 1} \left( \frac{(s_0 - d)\tilde{s} + (d + s_0)}{\tilde{s} - 1} U^{(r)}(\omega, \tilde{s}) - \mathbf{u}(\omega, a) \right) \\ &+ 2d \left( \frac{(s_0 - d)\tilde{s} + (d + s_0)}{\tilde{s} - 1} U^{(r)}(\omega, \tilde{s}) - \mathbf{u}(\omega, a) \right) - k^2 U^{(r)}(\omega, \tilde{s}). \end{aligned}$$

Inserting the series representation (3.10) and rearranging terms yields

$$\begin{aligned} p(\omega) &\left( \hat{u}^{(0)}(a) + (\tilde{s} - 1) \sum_{\ell=0}^{\infty} a_\ell(\omega) \tilde{s}^\ell \right) \\ &= \hat{u}^{(2)}(a) + \frac{s_0(\tilde{s} + 1) - d(\tilde{s} - 1)}{\tilde{s} - 1} \left( (s_0(\tilde{s} + 1) - d(\tilde{s} - 1)) \sum_{\ell=0}^{\infty} a_\ell(\omega) \tilde{s}^\ell - \mathbf{u}(\omega, a) \right) \\ &+ 2d \left( \hat{u}^{(1)}(a) + (s_0(\tilde{s} + 1) - d(\tilde{s} - 1)) \sum_{\ell=0}^{\infty} a_\ell(\omega) \tilde{s}^\ell - \mathbf{u}(\omega, a) \right) \\ &- k^2 \left( \hat{u}^{(0)}(a) + (\tilde{s} - 1) \sum_{\ell=0}^{\infty} a_\ell(\omega) \tilde{s}^\ell \right). \end{aligned}$$

Multiplying by  $(\tilde{s} - 1)$  and simplifying further gives

$$\begin{aligned} p(\omega) \left( (\tilde{s} - 1) \hat{u}^{(0)}(a) + (\tilde{s} - 1)^2 \sum_{\ell=0}^{\infty} a_{\ell}(\omega) \tilde{s}^{\ell} \right) &= (\tilde{s} - 1) \hat{u}^{(2)}(a) \\ &+ \left( (s_0(\tilde{s} + 1))^2 - (d(\tilde{s} - 1))^2 \right) \sum_{\ell=0}^{\infty} a_{\ell}(\omega) \tilde{s}^{\ell} - (s_0(\tilde{s} + 1) + d(\tilde{s} - 1)) \mathbf{u}(\omega, a) \\ &+ 2d(\tilde{s} - 1) \hat{u}^{(1)}(a) - k^2 \left( (\tilde{s} - 1) \hat{u}^{(0)}(a) + (\tilde{s} - 1)^2 \sum_{\ell=0}^{\infty} a_{\ell}(\omega) \tilde{s}^{\ell} \right). \end{aligned}$$

Comparing the coefficients, one obtains

$$(5.11) \quad \begin{aligned} p(\omega) (-\hat{u}^{(0)}(a) + a_0) &= -\hat{u}^{(2)}(a) + s_0^2 a_0 - d^2 a_0 - (s_0 - d) \mathbf{u}(\omega, a) \\ &\quad - 2d\hat{u}^{(1)}(a) - k^2 (-\hat{u}^{(0)}(a) + a_0), \end{aligned}$$

$$(5.12) \quad \begin{aligned} p(\omega) (\hat{u}^{(0)}(a) - 2a_0 + a_1) &= \hat{u}^{(2)}(a) + s_0^2(2a_0 + a_1) - d^2(-2a_0 + a_1) \\ &\quad - (s_0 + d) \mathbf{u}(\omega, a) + 2d\hat{u}^{(1)}(a) - k^2 (\hat{u}^{(0)}(a) - 2a_0 + a_1), \end{aligned}$$

$$(5.13) \quad \begin{aligned} p(\omega) (a_{\ell-1} - 2a_{\ell} + a_{\ell+1}) &= s_0^2(a_{\ell-1} + 2a_{\ell} + a_{\ell+1}) \\ &\quad - d^2(a_{\ell-1} - 2a_{\ell} + a_{\ell+1}) - k^2(a_{\ell-1} - 2a_{\ell} + a_{\ell+1}). \end{aligned}$$

Collecting the  $a_{\ell}(\omega)$  and the interior degrees of freedom in a vector  $\mathbf{u}$ , the equation for the interior degrees of freedom (5.1), the coupling equation (5.11), equation (5.12), and equation (5.13) for  $\ell = 1, \dots, L$  are written in matrix vector form:

$$(5.14) \quad p(\omega) M \mathbf{u}(\omega) = \left( s_0^2(\omega) C_2 + s_0(\omega) C_1 + S \right) \mathbf{u}(\omega).$$

**5.2. Two-dimensional waveguide case.** For simplicity we assume periodic boundary conditions in the  $y$  direction, which makes it easier to calculate a reference solution to measure the error.

$$(5.15) \quad \begin{aligned} p(\partial_t) u(t, x, y) &= \partial_{xx} u(t, x, y) + \partial_{yy} u(t, x, y) + 2d \partial_x u(t, x, y) - k^2 u(t, x, y) \\ \text{for } x \in \mathbb{R}, y \in [-b, b], t &\geq 0, \\ u(t, x, b) &= u(t, x, -b) \text{ for } x \in \mathbb{R}, t \geq 0. \end{aligned}$$

Denoting by  $M_y$  the  $n_y \times n_y$  mass matrix and by  $A_y$  the  $n_y \times n_y$  stiffness matrix, each with periodic boundary conditions, the finite element discretization of (4.1) on a Cartesian grid is given by

$$(5.16) \quad p(\omega) (M \otimes M_y) \mathbf{u}(\omega) = \left( (s_0^2(\omega) C_2 + s_0(\omega) C_1 + S) \otimes M_y + M \otimes A_y \right) \mathbf{u}(\omega)$$

with the Kronecker product  $\otimes$  and  $(n_x + 2L) \times (n_x + 2L)$  matrices  $M$ ,  $C_1$ ,  $C_2$ , and  $S$  as in (5.14). The  $(n_x + 2L)n_y$  vector  $\mathbf{u}(\omega)$  collects the degrees of freedom on the Cartesian grid.

A different interpretation of (5.16) is as follows. A semidiscretization of (4.1) in the  $y$  component yields a coupled system of size  $n_y$ ,

$$(5.17) \quad \begin{aligned} p(\partial_t) M_y u(t, x) &= M_y \partial_{xx} u(t, x) + 2d M_y \partial_x u(t, x) + (A_y - k^2 M_y) u(t, x) \\ \text{for } x \in \mathbb{R}, t &\geq 0, \end{aligned}$$

for the vector-valued function  $u(t, x)$ . Replacing in section 5.1 the scalar-valued  $u$  by the vector-valued  $u$ , one obtains (5.16).

Using the above Kronecker notation, an extension to three-dimensional waveguide problems would now be very simple.

**6. Time discretization.** For the Schrödinger equation,  $s_0(\omega)$  is chosen to be constant,  $s_0 = -1 - i$ . Hence the domain where the boundary condition requires the Laplace transform to be analytic is the set of points above the line bisecting the first and the fourth quadrants (cf. Figure 3.2). Transforming (5.14) back to time domain, one obtains

$$(6.1) \quad i\partial_t M\mathbf{u}(t) = s_0^2 C_2 \mathbf{u}(t) + s_0 C_1 \mathbf{u}(t) + S\mathbf{u}(t).$$

The trapezoidal rule approximation of (6.1) is given by

$$iM \frac{\mathbf{u}^{n+1} - \mathbf{u}^n}{h} = (s_0^2 C_2 + s_0 C_1 + S) \frac{\mathbf{u}^{n+1} - \mathbf{u}^n}{2}$$

for constant  $s_0 = -1 - i$ .

For the heat and drift-diffusion equations,  $s_0(\omega)$  is also chosen to be constant,  $s_0 = -1$ , such that poles of  $U(s)$  in the right half plane of  $\mathbb{C}$  are excluded (cf. Figure 3.4). Time discretization is done using a Runge–Kutta method. By setting  $\tilde{S} = C_2 - C_1 + S$  the Runge–Kutta approximation of (5.14) is given by

$$\begin{aligned} MY_i &= M\mathbf{u}^n + h \sum_{j=1}^s a_{ij} \tilde{S}Y_j \quad \text{for } i = 1, \dots, s, \\ M\mathbf{u}^{n+1} &= M\mathbf{u}^n + h \sum_{i=1}^s b_i \tilde{S}Y_i. \end{aligned}$$

In the numerical examples the Radau IIA method of order 5 with  $s = 3$  internal stages is used [16]. The coefficients  $a_{ij}$  and  $b_i$  are given in the Butcher tableau in Table 6.1.

TABLE 6.1  
Radau IIA method of order 5.

$\frac{4-\sqrt{6}}{10}$	$\frac{88-7\sqrt{6}}{360}$	$\frac{296-169\sqrt{6}}{1800}$	$\frac{-2+3\sqrt{6}}{225}$
$\frac{4+\sqrt{6}}{10}$	$\frac{296+169\sqrt{6}}{1800}$	$\frac{88+7\sqrt{6}}{360}$	$\frac{-2-3\sqrt{6}}{225}$
1	$\frac{16-\sqrt{6}}{36}$	$\frac{16+\sqrt{6}}{36}$	$\frac{1}{9}$
	$\frac{16-\sqrt{6}}{36}$	$\frac{16+\sqrt{6}}{36}$	$\frac{1}{9}$

For the Klein–Gordon equation, we choose  $s_0(\omega) = -\omega$ . When transforming back to time domain,  $\omega$  becomes  $\partial_t$ . Again we use the trapezoidal rule approximation, which yields

$$(6.2) \quad (M - C_2) \frac{\mathbf{u}^{n+1} - 2\mathbf{u} + \mathbf{u}^{n-1}}{h^2} = -C_1 \frac{\mathbf{u}^{n+1} - \mathbf{u}^{n-1}}{2h} + S \frac{\mathbf{u}^{n+1} + 2\mathbf{u} + \mathbf{u}^{n-1}}{4}.$$

**7. Numerical examples.** Numerical examples are presented for Schrödinger, heat, drift-diffusion, and Klein–Gordon equations. In each case the observed convergence in  $\Delta x$  and in the number of coefficients in the series expansion is given.

**7.1. Schrödinger equation.** Time discretization is done using the trapezoidal or implicit midpoint rule. For the Schrödinger equation on the real line a comparison with other methods implementing transparent boundary conditions is given.



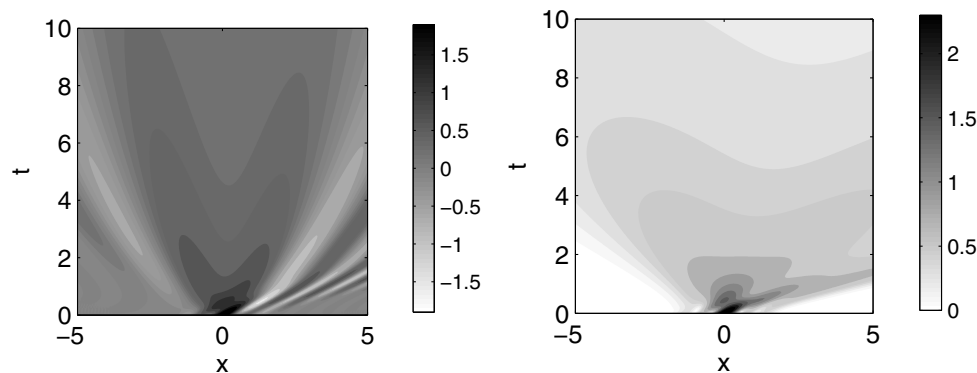


FIG. 7.1. Left: real part of the solution of the Schrödinger equation in the  $x-t$  plane. Right: modulus of the solution.

**7.1.1. One-dimensional case.** The exact solution for the Schrödinger equation  $ic\partial_t u = \partial_{xx} u$ , describing a single Gaussian beam that is traveling to the left or right with an angle  $r$ , is given by

$$u_q(x, t) = \sqrt{\frac{ci}{4t + ci}} \exp\left(\frac{-ci(x - x_0)^2 - cq(x - x_0) - q^2 t}{4t + ci}\right),$$

with  $q = c/2 \tan(r)$ ,  $r \in [-\pi/2, \pi/2]$ . In the example a superposition of three such beams is used. Hence the initial value is  $u(x, 0) = u_{q_1}(x, 0) + u_{q_2}(x, 0) + u_{q_3}(x, 0)$ , with angles given by  $r_1 = 1/6\pi$ ,  $r_2 = -2/7\pi$ , and  $r_3 = -7/17\pi$ . The analytic solution is thus given by

$$u_{\text{ref}}(x, t) = u_{q_1}(x, t) + u_{q_2}(x, t) + u_{q_3}(x, t).$$

Contour plots of the real part and of the modulus of the solution are shown in Figure 7.1.

The spatial  $l_2$  error at  $t = nh$  is defined by

$$(7.1) \quad e^n = \left( (\tilde{\mathbf{u}}^n - \Pi u_{\text{ref}}(x, nh))^T \tilde{M} (\tilde{\mathbf{u}}^n - \Pi u_{\text{ref}}(x, nh)) \right)^{1/2},$$

where  $\tilde{\mathbf{u}}^n$  is the coefficient vector of the finite element solution in the interior at time level  $n$ ,  $\tilde{M}$  is the mass matrix of the interior domain, and  $\Pi$  is the projection operator onto the finite element space. For  $c = 4$  the Schrödinger equation is integrated from  $t = 0$  to 10. The computational domain is the interval  $[-5, 5]$ . The angles are chosen such that the maximum of the fastest traveling beam reaches the boundary at about  $t = 2$ . The parameter in the Möbius transform is  $s_0 = -1 - i$  and we didn't optimize this choice.

In the experiments shown in Figure 7.2 finite elements of degree two are used. The mesh-width is  $\Delta x = 1/250$  and the step size  $h = 5 \cdot 10^{-6}$ . The left subplot shows the evolution of the error for various numbers of coefficients in the power series expansion (3.10). In the left of Figure 7.2 at about  $t = 1$  the error increases drastically if only few coefficients in the power series are used. This is due to the truncation error, which introduces reflections at the boundary, which are large for small values of  $L$ . In the right subplot the error is shown for several fixed  $t$ . This plot indicates that

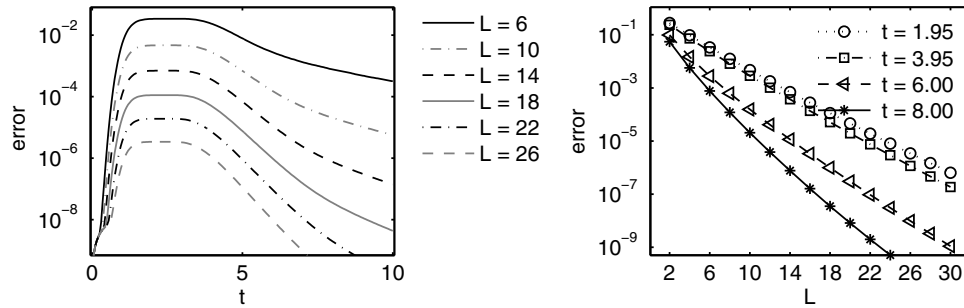


FIG. 7.2. Left: spatial  $l_2$  error over time for different  $L$  for quadratic finite elements with  $\Delta x = 1/250$  and  $h = 5 \cdot 10^{-6}$ . Right: spatial  $l_2$  error  $e^n$  at different times  $t = nh$  versus  $L$  for quadratic finite elements with  $\Delta x = 1/250$  and  $h = 5 \cdot 10^{-6}$ .

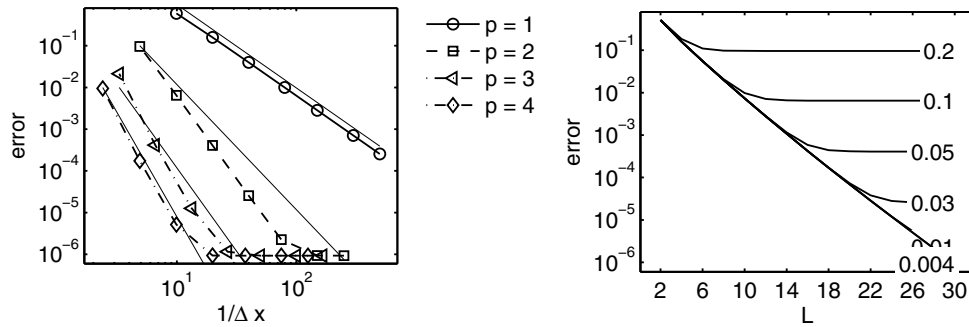


FIG. 7.3. Left: spatial and temporal  $l_2$  error versus the spatial mesh-width  $\Delta x$  for finite elements of degree 1, 2, 3, and 4. As a guide to the eye, lines with slope  $-2$ ,  $-3$ ,  $-4$ , and  $-5$  are included. Right: spatial and temporal  $l_2$  error versus  $L$  for different  $\Delta x$  obtained with quadratic finite elements and  $h = 5 \cdot 10^{-6}$ .

the truncation error introduced decays superalgebraically or even exponentially in the number of coefficients in the power series. This is an excellent result. With just a few additional degrees of freedom, a good quality transparent boundary condition is obtained. One has to compare the 20 additional degrees of freedom with the roughly 1000 degrees of freedom in the interior that are necessary in the case of finite elements of degree two to attain an error below  $10^{-4}$ ; cf. Figure 7.3.

In Figure 7.3 the  $l_2$  error with respect to time and space  $e = \sqrt{h \sum_n (e^n)^2}$  is shown. The left plot shows the error versus  $\Delta x$  for finite elements of degree  $p = 1, 2, 3, 4$ . Linear finite elements show the expected second order convergence. Quadratic finite elements show a fourth order convergence, which is one order better than expected. Finite elements of degree  $p = 3$  show a convergence that is slightly better than may be expected. As a guide to the eye, thin lines with a slope of  $-2$ ,  $-3$ ,  $-4$ , and  $-5$  are inserted. The number of coefficients in the power series is  $L = 30$ , and the temporal step size is  $h = 5 \cdot 10^{-6}$ . The right plot shows the error versus  $L$  for various  $\Delta x$  for quadratic finite elements. This shows, for example, that for  $\Delta x = 0.05$  the error saturates with  $L = 16$ .

**7.1.2. Comparison with other transparent boundary conditions.** To assess the efficiency of the pole condition, work-precision diagrams for the one-dimensional

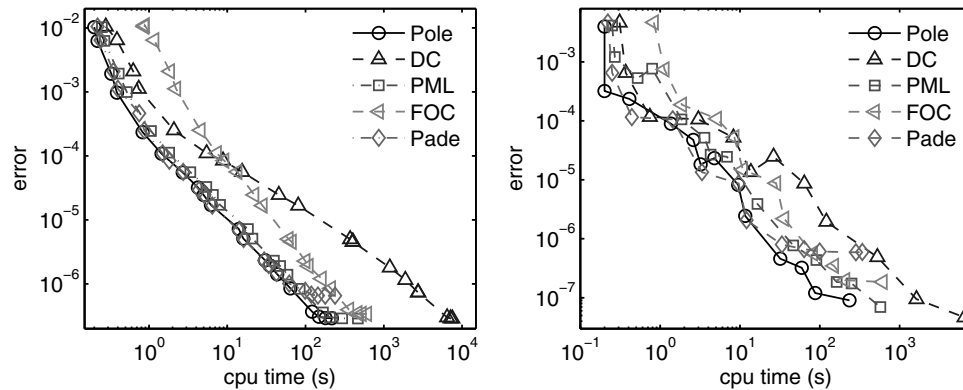


FIG. 7.4. Work-precision diagram comparing the pole condition, direct convolution, fast and oblivious convolution, Padé approximation of the  $\sqrt{\cdot}$ , and adaptive PML. Left: cubic finite elements. Right: quadratic finite elements.

Schrödinger example of section 7.1.1 are given in Figure 7.4, comparing the pole condition, the direct convolution (DC) [32, 1], the fast and oblivious convolution (FOC) [27, 23], a Padé approximation of degree 30 of the square root [20, 33, 2], and an adaptive PML method [2]. For high accuracies the quadratic operation count in the evaluation of the boundary condition starts to dominate the computational cost for the direct convolution. The fast and oblivious convolution shows a large computational overhead, whereas the adaptive PML method, the Padé method, and the pole condition method perform equally well. For the pole condition the number of coefficients in the power series expansion is  $L = 25$ . The rational Padé approximation uses 60 coefficients. The fast and oblivious convolution algorithm uses 51 quadrature points on hyperbolas and a basis  $B = 10$ . For the adaptive PML we have estimated the interior discretization error to be  $10^{-8}$ , the minimal and maximal wavelengths are estimated to be 0.1 and 10.

**7.1.3. Two-dimensional waveguide case.** The reference solution for the two-dimensional Schrödinger equation on an infinite strip with periodic boundary conditions, (5.15) with  $p(\partial_t) = ic\partial_t$  and  $k = d = 0$ , is given by

$$\sum_{j=-\infty}^{\infty} \frac{ci}{4t + ci} \exp\left(\frac{-ci(x^2 + (y - j2b)^2) - cqx - q^2t}{4t + ci}\right).$$

The series is truncated to  $j = -5, \dots, 5$ , such that the truncation error remains below the discretization error. The parameters are  $q = 3$  and  $c = 3.5$ . The Schrödinger equation is integrated for  $0 \leq t \leq 10$  on the domain  $[-3.5, 3.5] \times [-3.4, 3.4]$ , i.e.,  $b = 3.4$ , with transparent boundary conditions in  $x$ .

In Figure 7.5 the evolution of the error and the convergence in  $L$  for various  $t$  is shown.

Figure 7.6 shows the convergence with respect to the spatial discretization and the convergence in  $L$  for various spatial discretizations. The results are similar to the one-dimensional case.

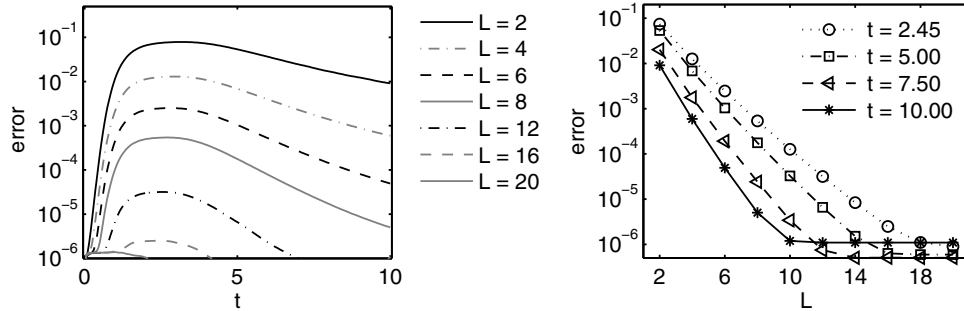


FIG. 7.5. Left: spatial  $l_2$  error over time for different  $L$  for quadratic finite elements with 200 grid points in the  $x$  and  $y$  directions ( $n_x = 400$ ,  $n_y = 400$  degrees of freedom) and  $h = 5 \cdot 10^{-4}$ . Right: spatial  $l_2$  error  $e^n$  at different times  $t = nh$  versus  $L$  for quadratic finite elements with 200 grid points in the  $x$  and  $y$  directions and  $h = 5 \cdot 10^{-4}$ .

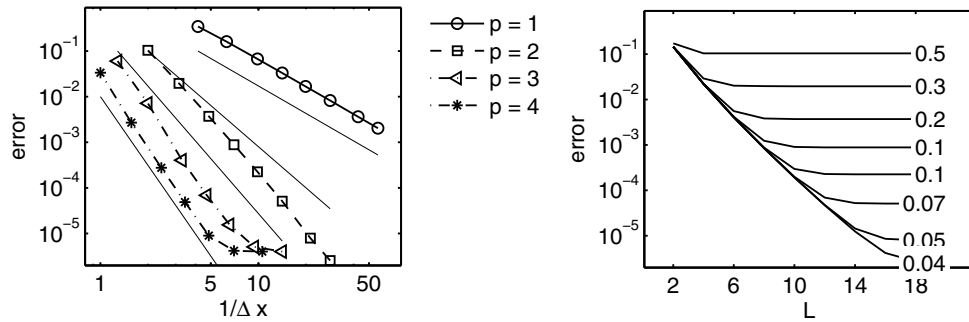


FIG. 7.6. Left: spatial and temporal  $l_2$  error versus the spatial mesh-width  $\Delta x$  for finite elements of degree 1, 2, 3, and 4. As a guide to the eye, lines with slope  $-2$ ,  $-3$ ,  $-4$ , and  $-5$  are included. Right: spatial and temporal  $l_2$  error versus  $L$  for different  $\Delta x$  obtained with quadratic finite elements and  $h = 5 \cdot 10^{-4}$ . In both cases discretization in  $y$  is done using the same number of degrees of freedom as for the  $x$  discretization.

**7.2. Heat equation.** The fundamental solution of the heat equation  $\partial_t u = \partial_{xx} u$  is

$$u(x, t) = \exp\left(-\frac{1}{2\sqrt{\pi t}} \frac{(x - x_0)^2}{4t}\right).$$

The heat equation is integrated from  $t = 0.02, \dots, 5$  on the interval  $[-5, 5]$  using the Radau IIA method of order 5. In the simulation the initial data are given by  $u_0(x) = u(x, 0.02)$ . Again the  $l_2$  error  $e^n$  at  $t_0 + nh$  is defined by (7.1) with  $u_{\text{ref}}(x, t_0 + nh) = u(x, t_0 + nh)$ . The parameter for the Möbius transform is  $s_0 = -1$ .

In the experiments shown in Figure 7.7 quadratic finite elements are used. The mesh-width is  $\Delta x = 1/250$  and the step size  $h = 10^{-3}$ . In the right subplot the error is shown for several fixed  $t$ . Again this plot indicates that the truncation error introduced decays superalgebraically or exponentially in the number of coefficients in the power series. The left subplot shows the evolution of the error for various numbers of coefficients in the power series (3.10).

In Figure 7.8 the  $l_2$  error with respect to time and space  $e = \sqrt{h \sum_n (e^n)^2}$  is shown. The left plot shows the error versus  $\Delta x$  for finite elements of degree  $p = 1, 2, 3, 4$ .

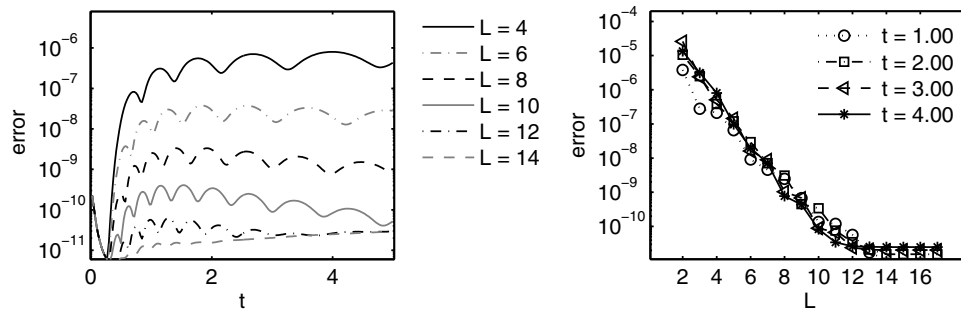


FIG. 7.7. Left: spatial  $l_2$  error  $e^n$  at different times  $t = nh$  versus  $L$  for quadratic finite elements with  $\Delta x = 1/250$  and  $h = 10^{-3}$ . Right: evolution of the error for different  $L$  for quadratic finite elements with  $\Delta x = 1/250$  and  $h = 10^{-3}$ .

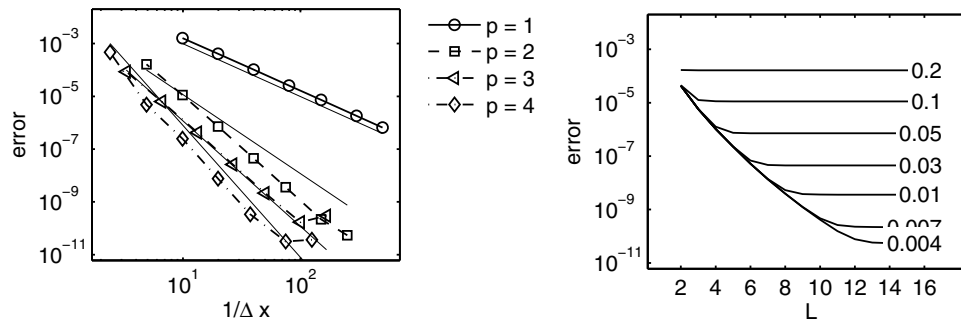


FIG. 7.8. Left: spatial and temporal  $l_2$  error versus the spatial mesh-width  $\Delta x$  for  $h = 10^{-3}$  and  $L = 17$ . Right: spatial and temporal  $l_2$  error versus  $L$  for different  $\Delta x$  obtained with quadratic finite elements and  $h = 10^{-3}$ .

Linear finite elements show the expected second order convergence. Again finite elements of degree  $p = 2, 3$  show a fourth order convergence. We assume that the unexpectedly good convergence property of the quadratic finite elements might be due to some symmetry in this special solution. The number of power series coefficients is  $L = 17$ , and the temporal step size is  $h = 10^{-3}$ . The right plot shows the error versus  $L$  for various  $\Delta x$  for quadratic finite elements.

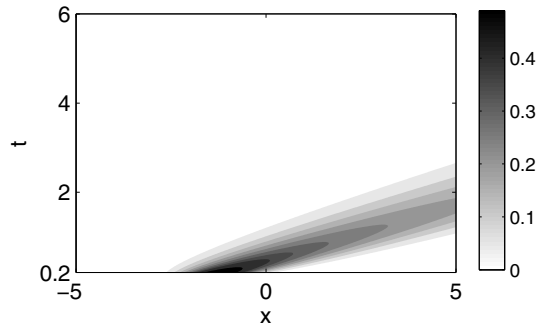
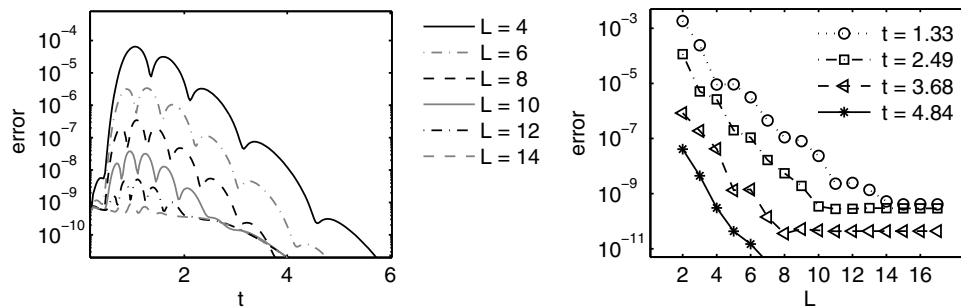
**7.3. Drift-diffusion equation.** The drift-diffusion example is integrated using a Runge–Kutta method, the Radau IIA method of order 5.

**7.3.1. One-dimensional case.** The fundamental solution for the drift-diffusion equation  $c\partial_t u = \partial_{xx} u + 2d\partial_x u$  is given by

$$u(x, t) = \frac{c}{\sqrt{4\pi t}} \exp\left(-\frac{c(x - x_0 + 2dt/c)^2}{4t}\right).$$

We set the initial time to 0.2,  $x_0 = 2$ ,  $d = -2$ , and  $c = 1$  and use  $u_0(x) = u(x, 0.2)$  as initial data to integrate the drift-diffusion equation for  $0.2 \leq t \leq 6$  on the interval  $[-5, 5]$ .

A contour plot of the solution is shown in Figure 7.9. Again the  $l_2$  error  $e^n$  at  $t_0 + nh$  is defined by (7.1) with  $u_{\text{ref}}(x, t_0 + nh) = u(x, t_0 + nh)$ .

FIG. 7.9. Solution of the drift-diffusion equation in the  $x-t$  plane.FIG. 7.10. Left: spatial  $l_2$  error  $e^n$  at different times  $t = nh$  versus  $L$  for quadratic finite elements with  $\Delta x = 1/250$  and  $h = 10^{-4}$ . Right: spatial  $l_2$  error over time for different  $L$  for quadratic finite elements with  $\Delta x = 1/250$  and  $h = 10^{-4}$ .

The results are similar to the ones obtained for the heat equation. In the experiments shown in Figure 7.10, quadratic finite elements are used. The mesh-width is  $\Delta x = 1/400$  and the step size  $h = 10^{-4}$ . The left subplot shows the evolution of the error for various numbers of coefficients in the power series (3.10). The parameters are such that the maximum of the solution hits the boundary at about  $t = 1.8$ . In the right subplot the error is shown for several fixed  $t$ . Again this plot indicates that the truncation error introduced decays superalgebraically or exponentially in the number of coefficients in the power series.

In Figure 7.11 the  $l_2$  error with respect to time and space is shown. The left plot shows the error versus  $\Delta x$ . Finite elements of degree  $p = 1, 3, 4$  show the expected order of convergence. Quadratic finite elements again show a convergence that is better than may be expected. The number of coefficients in the power series is  $L = 17$ , and the temporal step size is  $h = 10^{-4}$ . The right plot shows the error versus  $L$  for various  $\Delta x$  for quadratic finite elements.

**7.3.2. Two-dimensional waveguide case.** The fundamental solution for the two-dimensional drift-diffusion equation in a waveguide with periodic boundary conditions, i.e.,  $p(\partial_t) = \partial_t$  and  $k = 0$  in (5.15), is given by

$$\sum_{j=-\infty}^{\infty} \frac{1}{t} \exp \left( \frac{-((x - x_0 + 2dt)^2 + (y + 2jb)^2)}{t} \right).$$

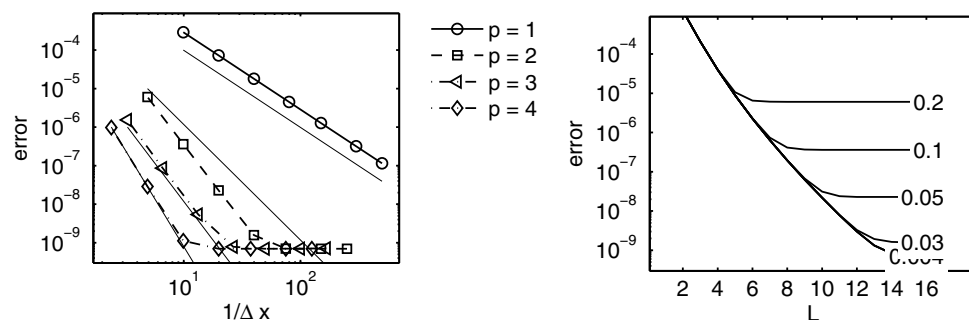


FIG. 7.11. Left: spatial and temporal  $l_2$  error versus the spatial mesh-width  $\Delta x$ . Right: spatial and temporal  $l_2$  error versus  $L$  for different  $\Delta x$  obtained with quadratic finite elements and  $h = 10^{-4}$ .

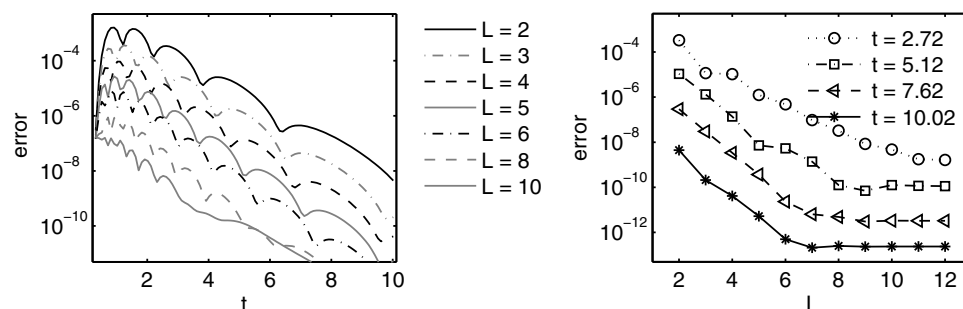


FIG. 7.12. Left: spatial  $l_2$  error over time for different  $L$  for quadratic finite elements with 200 grid points in the  $x$  and  $y$  directions ( $n_x = 400$ ,  $n_y = 400$  degrees of freedom) and  $h = 2 \cdot 10^{-2}$ . Right: spatial  $l_2$  error  $e^n$  at different times  $t = nh$  versus  $L$  for quadratic finite elements with 200 grid points in the  $x$  and  $y$  directions and  $h = 2 \cdot 10^{-2}$ .

For  $(x, y) \in [-5, 5] \times [-5, 5]$  and  $0.3 \leq t \leq 10$ , the series is truncated to  $j = -3, \dots, 3$ , such that the truncation error remains below the discretization error. The parameters are  $d = 1.3$  and  $x_0 = 1.3$  and the periodicity is  $b = 5$ .

In Figure 7.12 the evolution of the error and the convergence in  $L$  for various  $t$  is shown.

Figure 7.13 shows the convergence with respect to the spatial discretization and the convergence in  $L$  for various spatial discretizations. The left plot shows the error versus  $\Delta x$  for finite elements of degree  $p = 1, 2, 3, 4$ . The experiment shows the expected rate of convergence. The number of coefficients in the power series is  $L = 10$ , and the temporal step size is  $h = 2 \cdot 10^{-2}$ . The right plot shows the error versus  $L$  for various  $\Delta x$  for quadratic finite elements.

#### 7.4. Dispersive wave equation.

**7.4.1. One-dimensional case.** The dispersive wave equation or Klein–Gordon equation

$$c\partial_{tt}u(x, t) = \partial_{xx}u(x, t) - k^2u(x, t)$$

with parameters  $c = 1$ ,  $k = 4$ , and initial data  $u^0(x) = \exp(-x^2)$  is integrated from  $t = 0$  to  $t = 30$  on  $x \in [-5, 5]$ . The initial velocity is set to zero, which is

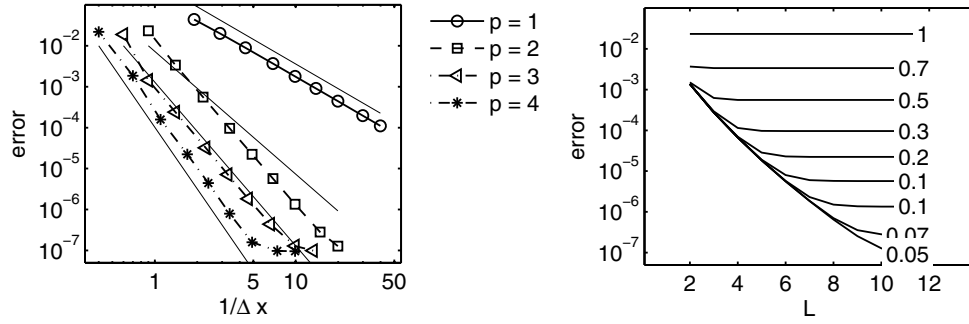


FIG. 7.13. Left: spatial and temporal  $l_2$  error versus the spatial mesh-width  $\Delta x$  for finite elements of degree 1, 2, 3, and 4. As a guide to the eye, lines with slope  $-2$ ,  $-3$ ,  $-4$ , and  $-5$  are included. Right: spatial and temporal  $l_2$  error versus  $L$  for different  $\Delta x$  obtained with quadratic finite elements and  $h = 2 \cdot 10^{-2}$ . In both cases discretization in  $y$  is done using the same number of degrees of freedom as for the  $x$  discretization.

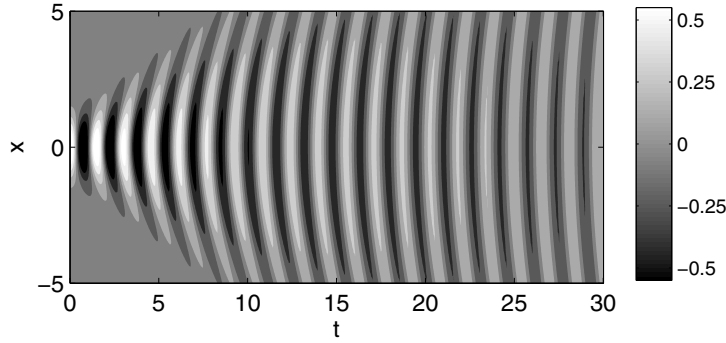


FIG. 7.14. Solution of the Klein-Gordon equation in the  $t-x$  plane.

approximated by setting  $\tilde{\mathbf{u}}^{-1} = \tilde{\mathbf{u}}^0 + h^2/2(\tilde{S}\tilde{\mathbf{u}}^0)$ . A contour plot of the solution is shown in Figure 7.14. As there is no analytic reference solution available, a reference solution  $\tilde{\mathbf{u}}_{\text{ref}}^n$  is computed on a domain three times larger,  $[-15, 15]$ , using the same spatial and temporal discretization and setting  $L = 30$ . This way only the error at the artificial boundary that originates from coupling the Laplace transform of the solution with the finite element discretization in the interior is measured.

Note that, as pointed out in section 5.1, Theorem 5.1, for the scalar wave equation on the real line, i.e., for  $k = 0$ , the equations for the  $a_j$  decouple and the exact transparent boundary  $\partial_\nu u = \partial_t u$  is obtained.

The error is measured in the energy norm given by

$$(7.2) \quad e^n = (\tilde{\mathbf{e}}_t^n)^T \tilde{M} \tilde{\mathbf{e}}_t^n + (\tilde{\mathbf{e}}^n)^T \tilde{A} \tilde{\mathbf{e}}^n,$$

where  $\tilde{\mathbf{e}}_t = (\tilde{\mathbf{e}}^{n+1} - \tilde{\mathbf{e}}^n)/2h$  is an approximation to the velocity, and  $\tilde{M}$  and  $\tilde{A}$  are the mass and stiffness matrices in the interior domain. The error vector is given by  $\tilde{\mathbf{e}}^n = \tilde{\mathbf{u}}^n - P\tilde{\mathbf{u}}_{\text{ref}}^n$ , where  $P\tilde{\mathbf{u}}_{\text{ref}}^n$  is the restriction of the reference solution to the degrees of freedom corresponding to the computational domain.

In Figure 7.15 the discretization parameters are  $\Delta x = 1/250$  and  $h = 2 \cdot 10^{-4}$ ; finite elements of degree two are used. The left subplot shows the evolution of the



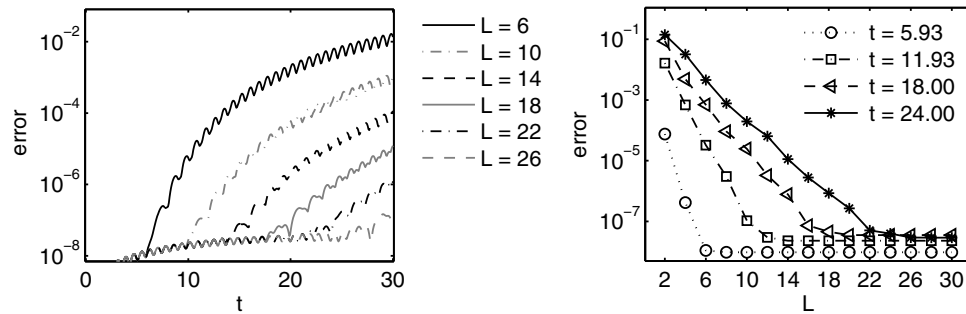


FIG. 7.15. Left: error  $e^n$  (7.2) at different times  $t = nh$  versus  $L$  for quadratic finite elements with  $\Delta x = 1/250$  and  $h = 2 \cdot 10^{-4}$ . Right: error in energy norm over time for different  $L$  for quadratic finite elements with  $\Delta x = 1/250$  and  $h = 2 \cdot 10^{-4}$ .

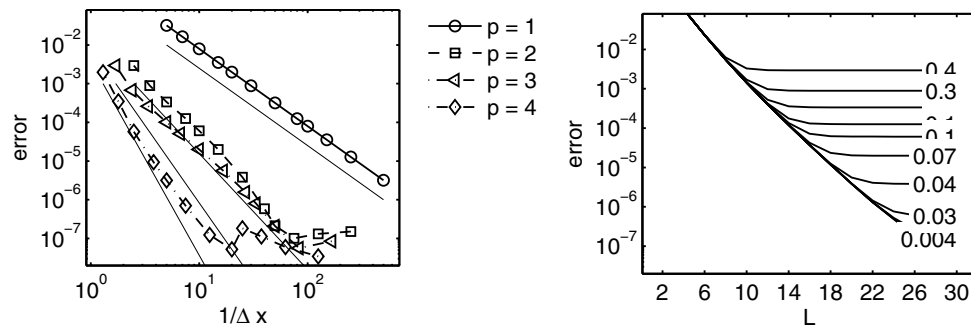


FIG. 7.16. Left: spatial and temporal  $l_2$  error over the spatial mesh-width  $\Delta x$ . Right: spatial and temporal  $l_2$  error versus  $L$  for different  $\Delta x$  obtained with quadratic finite elements and  $h = 2 \cdot 10^{-4}$ .

error for  $L$  ranging from 6 to 26. In the beginning the error is very small, as we are not measuring any  $\Delta x$  or  $h$  dependent discretization error of the interior but solely the error introduced by discretizing the boundary condition and truncating the power series expansion. The right subplot displays the error measured at several fixed  $t$  for different number of coefficients  $L$  in the power series expansion.

In Figure 7.16 we have plotted the spatial and temporal  $l_2$  error  $e = \sqrt{h \sum_n (e^n)^2}$  over  $\Delta x$  for finite elements of polynomial order  $p = 1, 2, 3, 4$ . The cubic finite elements show only a third order convergence, which is worse than one may have hoped for.

**7.5. Two-dimensional waveguide case.** The initial value for a dispersive wave equation in a periodic waveguide is given by  $u(x, y, 0) = \exp(-x^2 - y^2)$  for  $(x, y) \in [-4, 4] \times [-4, 4]$ . The initial velocity  $\dot{u}(x, y, 0)$  is set to zero. We set  $c = 1$  and  $k = 4$  and integrate

$$c \partial_{tt} u(x, y, t) = \partial_{xx} u(x, y, t) + \partial_{yy} u(x, y, t) - k^2 u(x, y, t),$$

$$u(x, b, t) = u(x, -b, t)$$

from  $t = 0$  to  $t = 20$ . The error in the energy norm is measured against a reference solution calculated on  $[-8, 8] \times [-4, 4]$  using the same spatial and temporal discretization and setting  $L = 24$ . As for the one-dimensional case in Figure 7.17 the evolution of the error and the convergence in  $L$  for various  $t$  are shown.

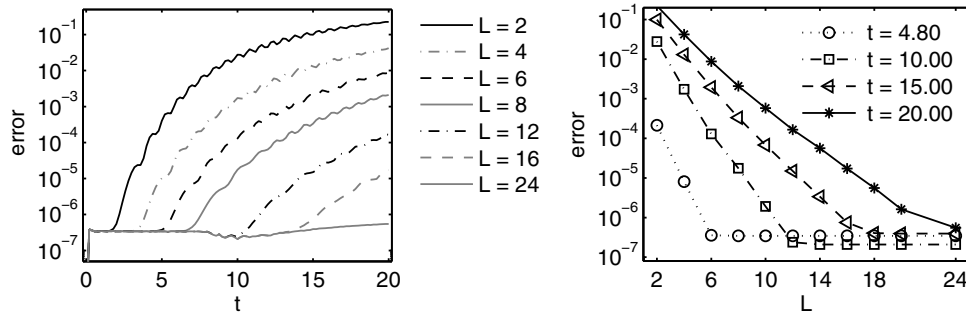


FIG. 7.17. Left: spatial  $l_2$  error over time for different  $L$  for quadratic finite elements with 250 grid points in the  $x$  and  $y$  directions ( $n_x = 400$ ,  $n_y = 400$  degrees of freedom) and  $h = 2 \cdot 10^{-3}$ . Right: spatial  $l_2$  error  $e^n$  at different times  $t = nh$  versus  $L$  for quadratic finite elements with 250 grid points in the  $x$  and  $y$  directions and  $h = 2 \cdot 10^{-3}$ .

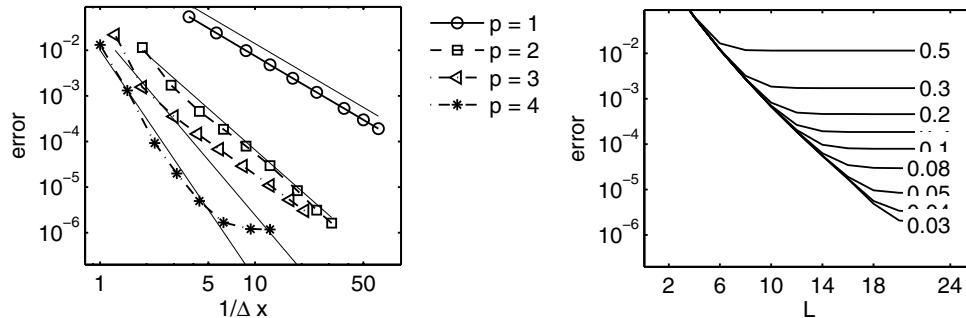


FIG. 7.18. Left: spatial and temporal  $l_2$  error versus the spatial mesh-width  $\Delta x$  for finite elements of degree 1, 2, 3, and 4. As a guide to the eye, lines with slope  $-2$ ,  $-3$ ,  $-4$ , and  $-5$  are included. Right: spatial and temporal  $l_2$  error versus  $L$  for different  $\Delta x$  obtained with quadratic finite elements and  $h = 2 \cdot 10^{-3}$ . In both cases discretization in  $y$  is done using the same number of degrees of freedom as for the  $x$  discretization.

Figure 7.18 shows the convergence with respect to the spatial discretization and the convergence in  $L$  for various spatial discretizations. As in the one-dimensional case an order reduction for finite elements of polynomial degree 3 is observed.

**8. Summary.** We described a new general approach to construct transparent boundary conditions for the dispersive wave, heat, Schrödinger, and drift-diffusion equations. The central idea of the pole condition is to distinguish between incoming/unbounded and outgoing/bounded exterior solutions by looking at the poles of the spatial Laplace transform. From this analysis it can be deduced that an exact transparent boundary condition requires the Laplace transform to be analytic in a certain domain in the complex plane, whereas the location of this domain depends on the equation. Using the pole condition it should be possible to derive transparent boundary for problems with inhomogeneous exterior domains.

It was shown that the well-known exact transparent boundary conditions are recovered with this ansatz by a special choice of parameters. To construct a numerical algorithm, the Laplace transform was represented as a power series on the unit disc, which then allowed the derivation of equations for the coefficients. The actual scheme

then computes a finite number of these coefficients, providing an approximate discrete transparent boundary condition. It has been shown in numerical experiments for all four equations that the error introduced by the boundary conditions decays exponentially fast in the number  $L$  of coefficients. The number of unknowns added to the system in order to realize the boundary condition was very moderate. In the one-dimensional case even for very fine spatial resolution in the computational domain (order of thousands of degrees of freedom), around 20 additional unknowns were sufficient to reduce the boundary error to the order of the discretization error in the interior.

Simulations for a two-dimensional waveguide problem were presented to point out how the method can be extended to the higher-dimensional case. We are currently working on an extension to general two-dimensional convex domains with a polygonal boundary.

#### REFERENCES

- [1] X. ANTOINE AND C. BESSE, *Unconditionally stable discretization schemes of non-reflecting boundary conditions for the one-dimensional Schrödinger equation*, J. Comput. Phys., 188 (2003), pp. 157–175.
- [2] X. ANTOINE, A. ARNOLD, C. BESSE, M. EHRHARDT, AND A. SCHÄDLE, *A review of transparent and artificial boundary condition techniques for linear and nonlinear Schrödinger equations*, Commun. Comput. Phys., 4 (2008), pp. 729–796.
- [3] A. ARNOLD AND M. EHRHARDT, *Discrete transparent boundary conditions for wide angle parabolic equations in underwater acoustics*, J. Comput. Phys., 145 (1998), pp. 611–638.
- [4] R. J. ASTLEY, *Infinite elements for wave problems: A review of current formulations and an assessment of accuracy*, Internat. J. Numer. Methods Engrg., 49 (2000), pp. 951–976.
- [5] J.-P. BÉRENGER, *A perfectly matched layer for the absorption of electromagnetic waves*, J. Comput. Phys., 114 (1994), pp. 185–200.
- [6] F. COLLINO, *High order absorbing boundary conditions for wave propagation models: Straight line boundary and corner cases*, in Proceedings of the 2nd International Conference on Mathematical and Numerical Aspects of Wave Propagation, R. Kleinman, T. Angell, D. Colton, F. Santosa, and I. Stakgold, eds., SIAM, Philadelphia, 1993, pp. 161–171.
- [7] G. DOETSCH, *Einführung in Theorie und Anwendung der Laplace Transformation*, 3rd ed., Birkhäuser Verlag, Basel, Stuttgart, 1976.
- [8] P. DUREN AND A. SCHUSTER, *Bergman Spaces*, Math. Surveys Monogr. 100, AMS, Providence, RI, 2004.
- [9] B. ENGQUIST AND A. MAJDA, *Absorbing boundary conditions for the numerical simulation of waves*, Math. Comp., 31 (1977), pp. 629–651.
- [10] D. GIVOLI, *High-order local non-reflecting boundary conditions: A review*, Wave Motion, 39 (2004), pp. 319–326.
- [11] D. GIVOLI AND B. NETA, *High-order non-reflecting boundary schemes for time-dependent waves*, J. Comput. Phys., 186 (2003), pp. 24–46.
- [12] T. HAGSTROM, *Radiation boundary conditions for numerical simulation of waves*, Acta Numer., 8 (1999), pp. 47–106.
- [13] T. HAGSTROM, *New results on absorbing layers and radiation boundary conditions*, in Topics in Computational Wave Propagation. Direct and Inverse Problems, M. Ainsworth, P. Davies, D. Duncan, P. Martin, and B. Rynne, eds., Lect. Notes Comput. Sci. Eng. 31, Springer-Verlag, Berlin, 2003, pp. 1–42.
- [14] T. HAGSTROM AND T. WARBURTON, *A new auxiliary variable formulation of high-order local radiation boundary conditions: Corner compatibility conditions and extensions to first order systems*, Wave Motion, 39 (2004), pp. 327–338.
- [15] E. HAIRER AND G. WANNER, *Solving Ordinary Differential Equations I*, Springer-Verlag, Berlin, Heidelberg, 1991.
- [16] E. HAIRER AND G. WANNER, *Solving Ordinary Differential Equations II*, Springer-Verlag, Berlin, Heidelberg, 1991.
- [17] E. HAIRER, CH. LUBICH, AND M. SCHLICHTE, *Fast numerical solution of nonlinear Volterra convolution equations*, SIAM J. Sci. Statist. Comput., 6 (1985), pp. 532–541.
- [18] T. HOHAGE AND L. NANNEN, *Hardy Space Infinite Elements for Scattering and Resonance*

- Problems*, Tech. Rep. 2007-17, Institut für Numerische und Angewandte Mathematik, Göttingen, 2007.
- [19] T. HOHAGE, F. SCHMIDT, AND L. ZSCHIEDRICH, *Solving time-harmonic scattering problems based on the pole condition I: Theory*, SIAM J. Math. Anal., 35 (2003), pp. 183–210.
  - [20] P. JOLY, *Pseudo-transparent boundary conditions for the diffusion equation. Part I*, Math. Methods Appl. Sci., 11 (1989), pp. 725–758.
  - [21] Y. KATZNELSON, *An Introduction to Harmonic Analysis*, 2nd ed., Dover, New York, 1968.
  - [22] E. LINDMAN, *Free space boundary conditions for the time dependent wave equation*, J. Comput. Phys., 18 (1975), pp. 66–78.
  - [23] M. LÓPEZ-FERNÁNDEZ, C. LUBICH, AND A. SCHÄDLE, *Adaptive, Fast and Oblivious Convolution in Evolution Equations with Memory*, ZIB Report 06-45, Zuse-Institute Berlin, 2006.
  - [24] C. LUBICH, *Convolution quadrature and discretized operational calculus I*, Numer. Math., 52 (1988), pp. 129–145.
  - [25] C. LUBICH, *Convolution quadrature and discretized operational calculus II*, Numer. Math., 52 (1988), pp. 413–425.
  - [26] C. LUBICH AND A. OSTERMANN, *Runge-Kutta methods for parabolic equations and convolution quadrature*, Math. Comp., 60 (1993), pp. 105–131.
  - [27] C. LUBICH AND A. SCHÄDLE, *Fast convolution for nonreflecting boundary conditions*, SIAM J. Sci. Comput., 24 (2002), pp. 161–182.
  - [28] A. SCHÄDLE, *Ein schneller Faltungsalgorithmus für nichtreflektierende Randbedingungen*, Ph.D. thesis, Mathematisches Institut, Universität Tübingen, Tübingen, Germany, 2002.
  - [29] A. SCHÄDLE, D. RUPRECHT, AND F. SCHMIDT, *Transparent boundary conditions—the pole condition approach*, in Proceedings of Waves 2007: The 8th International Conference on Mathematical and Numerical Aspects of Waves, N. Biggs et al., eds., University of Reading, Reading, 2007, pp. 301–303.
  - [30] F. SCHMIDT, *Solution of Interior-Exterior Helmholtz-Type Problems Based on the Pole Condition Concept: Theory and Algorithms*, habilitation thesis, Free University Berlin, 2002.
  - [31] F. SCHMIDT, *Pole condition: A new approach to solve scattering problems*, in Oberwolfach Report, Vol. 1, number 1, Mathematisches Forschungsinstitut Oberwolfach, EMS Publishing House, Zürich, 2004, pp. 615–617.
  - [32] F. SCHMIDT AND D. YEVICK, *Discrete transparent boundary conditions for Schrödinger-type equations*, J. Comput. Phys., 134 (1997), pp. 96–107.
  - [33] J. SZEFTTEL, *Design of absorbing boundary conditions for Schrödinger equations in  $\mathbb{R}^d$* , SIAM J. Numer. Anal., 42 (2004), pp. 1527–1551.
  - [34] S. TSYNKOV, *Numerical solution of problems on unbounded domains. A review*, Appl. Numer. Math., 27 (1998), pp. 465–532.